UNIVERSITY OF TWENTE.

Faculty of Surface technology and Tribology
Faculty of Precision Engineering
Master High tech systems and materials

The design of a microtribometer to measure sliding friction under rapid acceleration

Graduation project

Author:
Pepijn Rippen
s2014114

Daily supervisor:
Dr. Tanmaya Mishra
External supervisor:
Prof. dr. ir. Dannis Brouwer EngD
Supervisor:
Bas de Vries Msc.

Committee chair:
Prof. dr. ir. Matthijn de Rooij

Date:
June 27, 2025

Contents

Abstract

This paper presents the conceptual design of a microtribometer in a ball-on-flat contact configuration. The proposed setup is based on a precision-engineered loading mechanism designed to apply both normal and tangential forces with minimal inertia effects and parasitic motion. A dynamic analysis is carried out to understand how the system behaves during operation. Potential sources of measurement error and manufacturability constraints are then discussed to optimize the performance of the setup. Potential improvements and shortcomings are discussed for the current design, leading to a conclusion. Based on these insights, a novel measurement mechanism will be developed and evaluated for its effectiveness in capturing frictional behaviour under dynamic conditions with high accuracy.

Nomenclature

PZT Piezoelectric transducer

APA Ampified piezoelectric actuator

VCA Voice coil actuator

RSS Residual sum of squares

RMS Root mean square

DOF Degrees of freedom

PID Proportional-integral-derivative

FEM Finite elements method

1 Introduction

Friction—the resistance to relative motion between surfaces in contact— is a fundamental phenomenon in both natural and mechanical systems. The friction resulting from dynamic forces in these systems often leads to wear, degradation, and eventual failure of components. Rapid accelerations and impact loads in engineering systems can cause frictional instabilities such as stick-slip, squeal, and fretting fatigue. Numerous scientific and engineering domains revolve around the understanding and characterization of friction under dynamic conditions. Precision positioning systems used in, for instance, robotics and semiconductor manufacturing are primarily reliant on accurate friction models to design robust controllers that ensure accurate positioning. Additionally, the responsiveness and efficiency of hydraulic actuators, widely used in the aerospace, automotive and machine building industry, are strongly influenced by the frictional behavior along their seals and guiding elements under dynamic conditions. In contrast, in geological systems, sudden slip events in rock gouges reduce frictional strength, potentially triggering seismic activity. Similarly, the understanding of friction under dynamic conditions is also important in more everyday use cases like braking systems, where the friction between the brake pad and brake disc determines the deceleration characteristics and, thus, safety of the system itself.

Therefore, an accurate phenomenological characterization of friction under dynamic conditions is essential to anticipate or enhance system performance in both technological and natural systems, because to date, the aforementioned phenomena are not well understood. This has started extensive research on both advanced measurement techniques and more sophisticated friction models able to capture the complexity of frictional interaction under dynamic conditions. Studying friction under extreme dynamic conditions demands carefully controlled experiments and high-end instrumentation capable of capturing rapid frictional behavior.

1.1 Background

To date, there is no physics-based model that accurately describes friction under high dynamic conditions. For that reason, controlled laboratory studies must be conducted to isolate these properties and to find their influence on the coefficient of friction one by one. Being able to conduct such controlled studies that will yield repeatable outcomes, it is crucial to use a setup to measure frictional phenomena of which the control parameters are not only predictable and accurate, but also repeatable. Designing such a setup to characterize the coefficient of friction between two surfaces requires several key components.

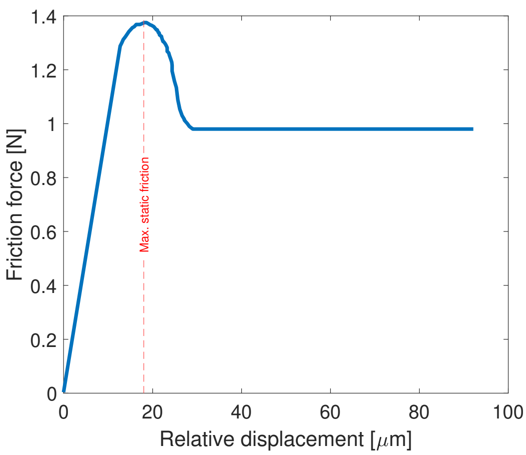

Figure 1: Illustration of friction versus relative displacement

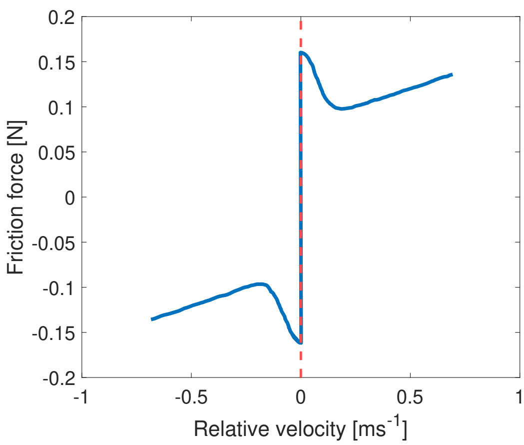

Figure 2: Illustration of friction versus sliding velocity

The foundational theory of contact mechanics was first introduced by Hertz [1], and later extended by Mindlin and Cattaneo which describes friction in the static and pre-sliding regime[2]. Coulomb and Amonton laid out three classical laws describing friction in the dynamic regime. See figure 1 and figure 2 for reference. These model assumptions allow for simplified predictions of friction under dynamic conditions at a macro scale. However, due to complex, real-world conditions such as material roughness, plasticity, and varying loads, purely theoretical models are often insufficient. While Coulomb's Third Law states that the kinetic coefficient of friction is velocity-independent, numerous experimental studies have observed behaviors that contradict this assumption under real-world conditions. The Stribeck effect, most prominent in lubricated contacts but also observed in dry contacts, shows a decrease in kinetic friction as the slip velocity increases [3]. This phenomenon can also be seen in figure 2 Velocity weakening and velocity strengthening are two other behaviours that defy Coulomb's Third law, proving that experimental investigations remain essential to fully capture the behavior of friction and wear under dynamic loading conditions [4].

There are a number of so-called state-variable models describing the dependence of velocity, meaning these models use internal variables to capture the friction behaviour over time. One of these models is the Lund-Grenoble - LuGre - model. This model is based on concept where friction between two surfaces is defined as the deflection of microscopic elastic bristles connecting the two surfaces. The friction under dynamic conditionsis proportional to the deflection of these bristles. Using this model, the friction force is calculated as follows [5].

$$F = \sigma_0 z + \sigma_1 \frac{dz}{dt} + \sigma_2 v \tag{1}$$

Here, z is the deflection of the bristle, σ_0 represents the bristle stiffness, σ_1 represents the energy dissipation during bristle deflection and σ_2 is the viscous friction coefficient representing viscous effects. The state equation $\frac{dz}{dt}$ is defined as follows.

$$\frac{dz}{dt} = v = \frac{\sigma_0 |v|}{g(v)} z \tag{2}$$

Where v is the relative velocity between the surfaces and g(v) is the Stribeck function, defined as

$$g(v) = F_c + (F_s - F_c) e^{-\left(\frac{v}{v_s}\right)^2} \tag{3}$$

Where F_c is the Coulomb friction, F_s is the static friction and v_s is the Stribeck velocity.

There is also a more simplified precursor to the LuGre model called the Dahl model. This model is able to capture hysteresis and pre-sliding, but not the Stribeck effect.

The friction force in the Dahl model is defined as follows[6].

$$\frac{dF}{dt} = \sigma_0 v \left(1 - \frac{F}{F_c} sgn(v)\right)^{\alpha} \tag{4}$$

Here, F is described as

$$F = \sigma_0 z \tag{5}$$

where the deflection state is defined as

$$\frac{dz}{dt} = v - \frac{\sigma_0 |v|}{F_c} z \tag{6}$$

As opposed to assuming an average bristle stiffness for the contact patch, the Generalized Maxwell Slip - GMS - model assumes a parallel connection of many flexural elements with each its own state parameters. This allows for a more accurate representation of local friction and sliding behaviour with the drawback of computational cost. The GMS model for a single element is defined as follows. The friction force F_f generated by the element is primarily due to the elastic deformation of the bristle. This is defined as

$$F_f = kx \tag{7}$$

In some forms, damping is added to the bristle deformation, which would then look like

$$F_f = kx + c\dot{x} \tag{8}$$

The slip rate $\dot{z}$, is a function of the relative velocity of the contact and the Stribeck force. It is defined as

$$\dot{z} = \dot{x} - \frac{k|\dot{x}|}{F_{Stribeck}(\dot{x})} z \tag{9}$$

Here, $F_{Stribeck}(\dot{x})$ is the steady-state friction force as a function of relative velocity, defined as

$$F_{\text{Stribeck}}(\dot{x}) = \left(F_c + (F_s - F_c) e^{-|\dot{x}/V_s|^{\delta}} \right) sgn(\dot{x}) \tag{10}$$

Here, F_s is the static friction force, F_c the Coulomb friction, V_s the Stribeck velocity, δ an exponent usually defined as 1 or 2 and $sgn(\dot{x})$ is the signum function which makes sure the friction force opposes the direction of the motion.

The described models each have their strengths and weaknesses, but identifying the system paremeters for validation of the model requires intricate experimentation. The system parameters for these models often rely on more than the conditions which are not defined in the model like temperature, wear and humidity, making the described models non physics based, but phenomological.
Figure 3 shows the three models plotted. The parameters used are for reference to compare how each model behaves. Looking at the Dahl model, it becomes indeed clear that this model displays a linear increasing friction force with increasing displacement, meaning there is no velocity dependecy, making it only suitable for idealized pre-sliding modelling. Looking at the LuGre model, it shows that the Stribeck effect is captured well. The GMS model displays the same characteristics as the LuGre model, but this depends on the configuration of the different bristles in the contact. On top of that, although these friction models show a degree of velocity-depence in the static and quasi-static friction regime, they are not suitable to model friction under dynamic conditions, relating acceleration and higher order effects to the change in friction. These models are yet to be developed.

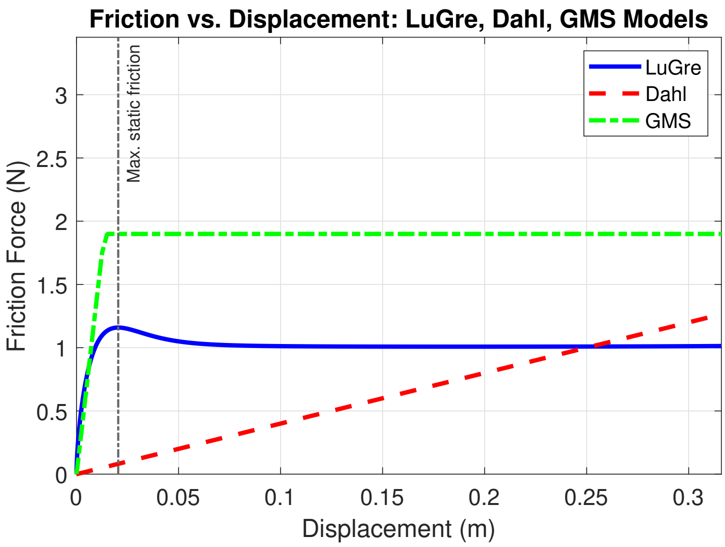

Figure 3: Comparison of LuGre, Dahl and GMS model

1.2 Literature review and state of the art

There are many studies found investigating friction in the static and quasi-static regime, only considering dependence on a constant sliding velocity. There is however no research specifically aimed at characterizing the dependence of changing sliding velocity or even changing acceleration in a contact. To capture such behaviour, one would use something called a tribometer, A testing rig designed to execute and measure a number of different friction tests. There are setups readily available, capable of doing friction testing under dynamic conditions, but the range in which these tests can be executed is limited. There are several off-the-shelf tribometers available that offer some capability in oscillatory friction testing, but none of these setups offer the opportunity to pick and choose a linear increasing velocity over a certain distance for instance [7][8][9].

There have been some studies with in-house built tribometers that somewhat test friction under dynamic conditions. Available research varies between quasi-static adhesion testing[10], sliding friction testing [11] or fretting fatigue wear testing[12][13]. However, these setups do not offer a wide range of stroke, normal force, sampling frequency for the friction measurement. Additionally, none of these setups are focused on high dynamics but rather low sliding velocities and low reciprocating frequencies, essentially evading high dynamic motion.

Given the lack of affordable commercial solutions and the absence of published studies using setups capable of wide-range, high-dynamic sliding friction measurements, a custom setup must be developed. Looking at similar built tribometers, a number of key instruments must be incorporated to ensure accurate and repeatable results.

For a tribometer capable of measuring friction under high dynamic conditions and deliver accurate and repeatable results, it is essential that it consists of

- A force transducer to apply and maintain a normal load onto the contact
- A force transducer applying a tangential load to one of the specimen, facilitating accelerated or constant slip
- A guiding mechanism allowing slip at the contact tangential to the normal load direction.
- High frequency and accuracy position sensing in the sliding part of the rig.
- High frequency and accurate friction force sensing at the contact.
- High frequency and accurate normal load measurement

1.3 Research questions, aims and objectives

As is mentioned before, friction under dynamic conditions is not well understood. To get a better understanding and to be able to characterize friction under high dynamic conditions, a setup must be developed that is able to subjecting a contact to high dynamic conditions whilst capturing the frictional behaviour as a result. Therefore, the main research goal of this thesis is to develop a theoretical design of a friction setup that is able to accurately measure the friction at a contact under dynamic conditions. The research question that follows from this is 'What must be considered for designing a friction setup able to accurately measure the friction at a contact under high accelerated sliding?'.

To reach this goal and effectively answer the research question, it is vital to investigate what types of instrumentation is necessary to achieve the main research goal, but moreover which options are there to choose from.

During the design process, it is important to consider what the contributing errors are to the eventual proposed solution and whether these errors fall within acceptable margins or not.

- How can a positioning mechanism can be used to allow for sliding and normal loading in a single grain contact?
- What actuators can be used to apply rapid accelerated sliding and apply normal load?
- What type of sensors are suitable for measuring friction, rapid acceleration and normal load?

- What the contributing errors are of the proposed design and how can these be quantified and minimized?

The primary objective of the designed setup is to measure friction under dynamic conditions in a sphere-on-flat contact configuration. A spherical specimen is subjected to a controlled normal force while in contact with a force-controlled flat specimen. Since direct friction measurement at the exact contact point is impractical, alternative methodologies must be used to accurately determine the frictional forces based on the applied normal load and the velocity profile of the flat specimen over time.

In this report, a theoretical design is presented for measuring friction under dynamic conditions in the context of earthquake characterization and fretting fatigue. A wide range of tribological experiments are required to investigate the behavior of friction under dynamic conditions, which depends on parameters such as velocity, acceleration, material plasticity, surface roughness, and normal load. To obtain repeatable experimental data, it is essential to maintain precise control over these parameters.

The proposed setup is based on a ball-on-flat contact configuration for friction under dynamic conditions. This configuration is chosen because such a contact geometry is well defined and not subject to alignment errors. Key controlled parameters include the applied force on the flat specimen—defining its time-dependent velocity—the normal force on the spherical specimen, the specimen diameter, and the elastic and plastic properties of the materials. Flexure mechanisms are employed to allow the necessary displacements while minimizing additional tribological influences unrelated to friction under dynamic conditionsitself [14]. Actuators are used to independently apply normal force to the contact surfaces and to drive the horizontal motion of the flat lower specimen. Position sensing is put in place to accurately monitor the displacements, velocity and acceleration in the contact. For measuring the friction force between the contacting surfaces, which will lead to the derivation of the coefficient of friction, a flexure combined with a position sensor is implemented to use as a force transducer. Key considerations to look out for when selecting actuator and sensor types is the accuracy and repeatablility in positioning and sensing that can be achieved depending on the loading conditions[15].

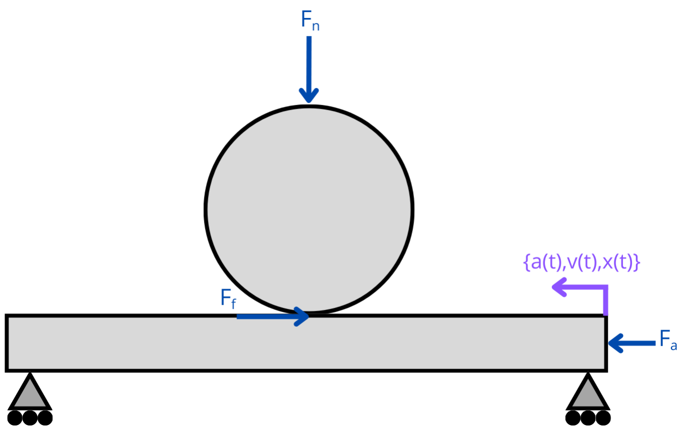

Figure 4: Schematic forces and displacement of ball on flat contact

The design prioritizes high system stiffness while minimizing mass, effectively minimizing elasticity and inertia effects. This ensures efficient transmission of force to the contact surface and allows for accurate measurement of friction under dynamic conditions. In addition, potential sources of measurement error and manufacturing constraints will be analyzed to optimize the performance of the setup, which will lead to a theoretical error of the setup.

1.4 Research approach

Research starts by defining a clear set of requirements for the experimental setup. These include the required range of sliding velocities, the range of applied normal loads, and the accuracy required for position and force measurements. These requirements describe what the setup must be able to measure and what conditions are needed to do so reliably. See figure 5 for reference to the design process.

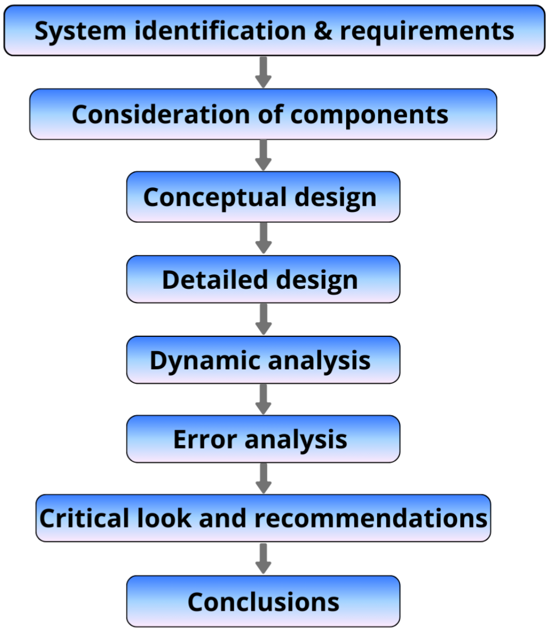

Figure 5: Flow chart of research process

Once the requirements are defined, the next step is to identify the components needed to meet them. The setup for measuring friction under dynamic conditions in a ball-on-flat sliding contact involves several key parts. For each part, different options are available. The benefits and drawbacks of each option are considered, leading to the creation of an initial design plan.

This initial design describes the main components of the system and how they will be used. It includes decisions about where sensors will be placed, how the loading and positioning mechanisms will work, and which components are suitable to meet the requirements.

After this, the detailed design is made. This involves a closer look at the selected components to decide if they are suitable, or if changes are needed to improve their performance.

A dynamic analysis is then carried out to understand how the system behaves during operation. This helps identify any vibrations that may occur and what might be causing them. After the design is finalized, an error analysis is done to estimate the overall uncertainty in the system. Knowing the possible sources of error is important to judge whether the accuracy is acceptable, or if further improvements are needed.

In the final step, the design is reviewed critically. Possible improvements and current limitations are discussed to provide a clear overview of the setup and its performance.

2 Requirements

Before the start of the design process, some requirements have to be made to make clear the boundaries in which the friction setup should be able to operate. Certain design choices follow from these requirements, leading to an initial and final concept.

2.1 Given requirements

Initial velocity range There should be an initial velocity to ensure the stick behaviour between the specimen and the substrate is left out during the measurement. Once the initial velocity is reached, the measurement will start. A very low initial velocity is sufficient while also desired, as the actuator used to move the substrate will have limited stroke. A range between 1 and $100\mu ms^{-1}$ is sufficient.

Final velocity range The final velocity range for the setup is in part dependent on the acceleration that should be achieved. To keep a wide range, it is set to 0.001 to $0.1ms^{-}1$.

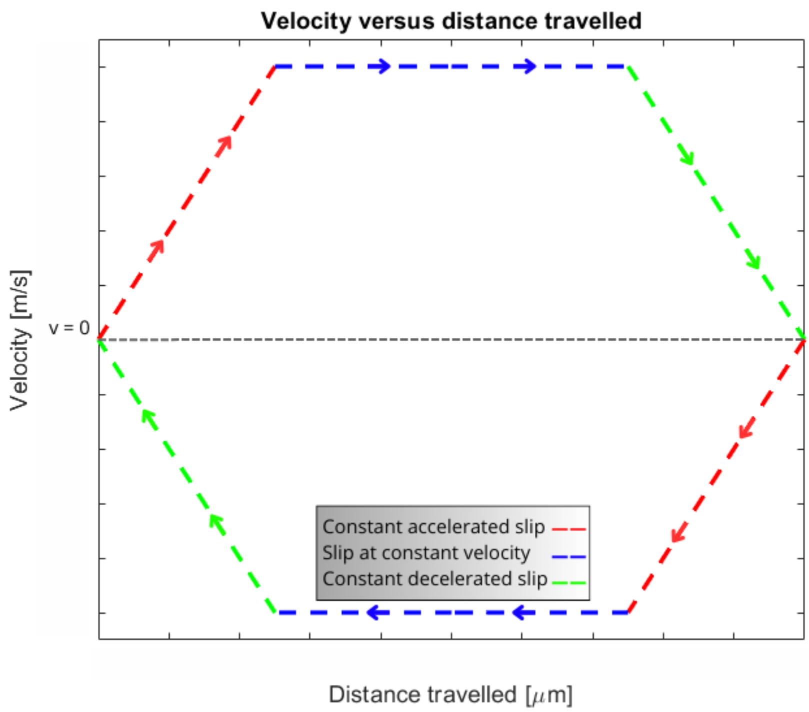

Figure 6: Recirpocating movement of lower flat substrate

Temperature and humidity The friction setup will operate in open air in the lab it is put in. This means that the temperature and humidity at that time will be the operating conditions for the friction setup.

Acceleration The acceleration that must be achieved is 10g at the higher end. Getting this done is a challenge because a certain mass must be moved with the desired acceleration. The higher the mass, the higher the force required for the actuator that is chosen to reach this acceleration. Therefore, it is important to keep the weight of the moving mass as low as possible.

Accuracy In the design process, parts will be incorporated that will each add an error to the readout in both position and force. The total error in the system will be an accumulation of these individual errors. Since this is about the design of a precision friction setup, the aim is to keep the error in applied normal load, friction force measurement and distance travelled within 1% of the measured quantity.

Glass bead diameter The spherical specimens used in this setup vary in size from a small diameter of 50 μm to a large diameter of 500μm. The flat lower specimen that is used is 30x15mm in width. Both specimens are made of soda lime glass [16], but can also be made of other materials. In the setup, the spherical specimen will be loaded on the flat bottom specimen with a normal load F_n. While the two specimen are in contact, the flat bottom specimen is then moved in the x-direction with a velocity $v_{desired}$.

2.2 Derived requirements

Normal load The normal load F_n is applied to the specimen, which will then press onto the substrate. The required load for the specimen is derived from the normal stress applied on two ring-shaped granular assemblies sandwiched between two ring shaped plates in rotary sliding contact. See figure 37 for reference. If the 8 MPa situation is taken, a required normal load between 0.1 and 10 N would be sufficient to apply the load necessary to achieve this normal stress.

Travel during accelerated slip To emulate the behaviour of two individual grains in contact in the granular assembly, the maximum distance these grains can be in contact with each other during a constant accelation phase, or in other words, accelerated slip from v_1 to v_2 is determined by the diameter of contact of the contacting solids. The maximum distance a grain-on-grain contact can be in contact is twice the contact diameter. Figure 9 gives a reference of the contact diameter, depicted as 2a in the picture. This means that the maximum sliding distance of twice the contact diameter is defined as 4a. Figure 7 is a schematic representation in a sliding configuration.

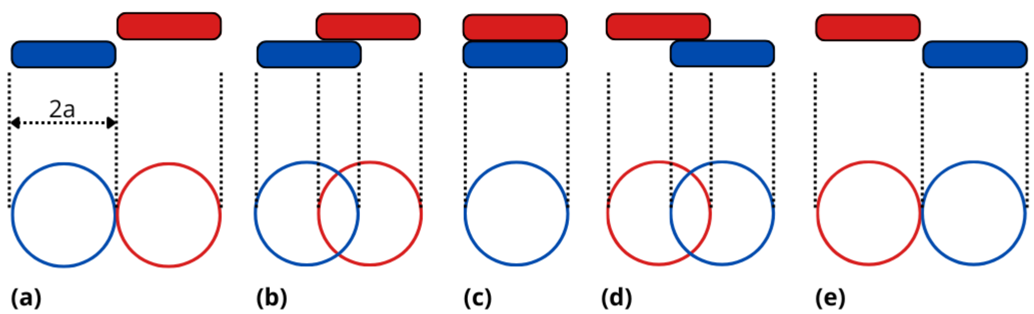

Figure 7: Schematic view of the contact patch of a ball-on-flat contact

Contact diameter The contact diameter of a Hertzian contact between a sphere and a flat surface is determined as follows. Note that the configuration in the setup is a sphere on sphere contact. The setup that is designed will consist of a spherical specimen loaded on a flat specimen. This is done for convenience, as it is difficult to load two individual spherical specimen in sliding contact. On top of that, both a sphere-on-sphere contact and a sphere-on-flat contact are forms of point contacts and will thus behave similarly.

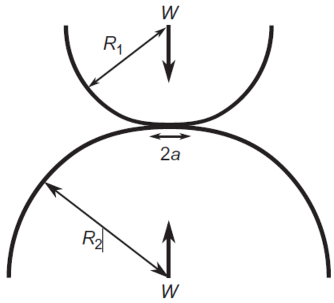

Figure 8: Schematic view of grain on grain contact

The estimation of the contact radius of a Hertzian sphere-on-flat contact is defined as

$$a = \left(\frac{3WR}{4E*}\right)^{\frac{1}{3}} = \left(\frac{3WR}{4\left(\frac{1-\nu_1^2}{E_1} + \frac{1-\nu_2^2}{E_2}\right)^{-1}}\right)^{\frac{1}{3}} \tag{11}$$

Here, a is the radius of the contact, W is the applied normal force, R the radius of the sphere and E* is the reduced Young's modulus of the contact. For a 50 μm bead and 0.063N load, the contact diameter equals 13.68μm, meaning the allowed travel during velocity jump would be 27.36 μm. For a 500 μm bead and 6.283N applied normal load, the allowed sliding distance would be 126.9 μm. When the contact radius is known, the contact pressure and maximum contact pressure can be defined as follows [17]:

$$p(r) = p_0\left(1 - \frac{r^2}{a^2}\right)^{0.5} \tag{12}$$

where p_0 is defined as $$p_0 = \frac{3W}{2\pi a^2} \tag{13}$$

Using equation 11, the relationship between the range of normal load, bead radius and the resulting contact diameter is described. The result is plotted in figure 9.

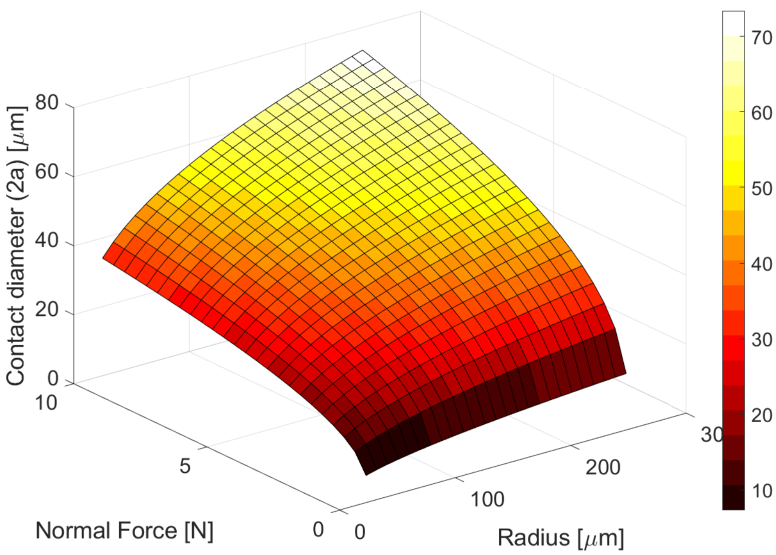

Figure 9: Surface plot showing the relationship between Normal force applied, bead diameter and resulting contact diameter.

Fatigue limit The flexures in the system should last 10 years. Together with the aforementioned, the requirement on the amount of cycles the flexures must endure is based on the number of back-and-forth reciprocation during one measurement and the frequency at which measurements are performed. It is estimated that 5000 cycles are needed per measurement. Doing an average of three measurements per week for 10 years would mean that the flexures must endure for 7.8 million cycles over a period of 10 years.

Stroke length in x-direction The required maximum stroke length of the stage that moves the lower flat specimen in the x-direction is determined by the desired velocity profile for the largest diameter specimen that is used. This velocity profile is divided in three sections: constant acceleration for twice the contact diameter, contant velocity of minimum 20 μm and maximum 100 μm, followed by constant deceleration of twice the contact diameter. These three stages are repeated in the opposite direction, resulting in the velocity profile plotted in figure 6. Added up, this results in that the flexure and actuator for the x-direction must make 200μm to 250 μm one way maximum, taking into consideration that there is a transition time between the constant acceleration, constant velocity and constant deceleration phase. On the lower end, this total sliding distance would be

2.3 Criteria for new setup

The requirements that are set will in part determine the components and dimensions for the setup that is to be designed. The determined requirements are listed in table 2.3.

Requirement	Value
Initial velocity range	1-100$\mu m s^{-}1$
Final velocity range	0.001 - 0.1 $ms^{-}1$
Normal load	0.1-10N
Temperature and humidity	Ambient temperature and 35-70% RH
Travel during velocity jump	20 - 100μm
Acceleration	0.5 - 10g
Accuracy horizontal movement	1% of distance travelled
Stroke length of x-stage	500μm
Glass bead diameter	50 - 500 mum
Lifetime	10 years
Normal Force accuracy	1% of applied normal force
Friction force accuracy	0.1% of applied normal force

3 Conceptual design

Once the system requirements are established, the necessary components and instrumentation to fulfil the requirements must be identified. This starts with determining the functional requirements of the machine to be able to determine what components are needed for every function. The flow chart in figure 10 shows the basic functionality of the setup, with the final goal of determining the coefficient of friction at the contact.

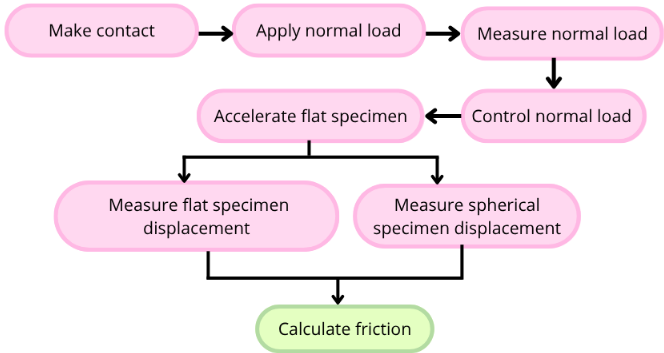

Figure 10: Flow chart of basic setup functionality

3.1 Choice of components

3.1.1 Positioning

A linear 2 DOF setup must be designed to facilitate both the normal load of the spherical specimen and the movement of the flat specimen. Either two decoupled 1 DOF positioning mechanisms can be used, or a single 2 DOF positioning mechanism. Two independent 1 DOF mechanisms are chosen to be designed for the following reasons.

- Modularity, offering opportunity for changing out components in the setup without having to redesign or replace the whole setup.
- Reduced crosstalk between axes due to independent positioning of degrees of freedom.
- Better control over errors arising. Isolating and minimizing errors becomes easier due to relative independence of movement axes and measurement thereof.
- Reduced moving mass per degree of freedom, aiding in fast response and low force required for achieving high acceleration.

The disadvantages of this configuration are:

- More components, meaning more misalignments
- More sensors present, meaning a higher cumulative error.

Several mechanisms can be considered for positioning. Options could be flexures combined with actuators, linear stages or air bearing stages. Linear stages based on guide rails would induce additional frictional effects due to the contact in the rails, introducing undesired unpredictability into the system. Promising options without having frictional losses or hysteresis and backlash are flexures or air bearings.
Air bearings use a continuous flow of sterile air to create a thin boundary layer of pressurized air between surfaces, causing the top surface to hover over the bottom surface. This principle is used to offer close to frictionless, backlash free and hysteresis free positioning with the possibility of sub-nanometer positioning.

Despite the promising capabilities of air bearings or air bearing stages, there are some drawbacks. The design of an air-bearing mechanism is complex. On top of that, the cost is relatively high with a typical price of a few thousand euros per stage if bought off-the-shelf, let alone designing it in-house. Lastly, with the introduction of high dynamic horizontal sliding combined with a normal load, this will cause the boundary layer to compress and induce unstable behavior. This could be minimized by using feedforward control in the supplied airflow at the cost of added complexity. Lastly, the setup will be in open air, meaning that contamination of the hovering surfaces is imminent, diminishing the performance of the air bearing. For that reason, flexures are chosen to facilitate the positioning in the setup.

Flexures offer a relatively low-cost, easy to design solution for linear positioning with high determinism, no hysterysis and no backlash, aiding the accuracy and repeatability. A simple parallel leaf spring could work to facilitate the motion for pre-loading the ball on flat contact. A parallel leaf spring would also be an option for the horizontal motion of the flat substrate. If designed correctly, the errors arising from the quasi-linear motion of the parallel leaf springs can be low enough to meet the accuracy requirements.

3.1.2 Actuation

Two actuators are needed in the setup. One is used to deliver the required normal load through a flexure onto the contact. Another actuator is used to deliver the sliding motion through a flexure onto the flat specimen. Common chosen options are linear stages, voice coil linear actuators or piezo actuators.

Linear stages bought off the shelf are often reliable in terms of repeatability and accuracy, but can seldom deliver the acceleration required for the setup. On top of that, many linear stages are bearing- or gear-based, introduction unwanted tribology, hysteresis and backlash.

A voice coil linear actuator works on the principle of Lorentz force, where a current running through a conducting medium results in a magnetic field able to apply force onto ferrous media present in that magnetic field. The current applied in a voice coil linear actuator is directly proportional to the applied load to the ferrous medium, making voice coil actuators highly deterministic. Another advantage of using voice coil actuators is that they do not have any stiffness themselves. The ferrous moving mass in the coil is floating, making the force applied from the coil decoupled from the frame the coil is mounted on, aiding in minimizing parasitic motion. One drawback is the need for a controller to compensate for temperature-induced variability, making the coil not exactly deterministic. A simple PID controller can mitigate this effect. Flexure shortening does not induce stress accumulation due to the actuator's mechanical decoupling from the frame. Instead it will lead to an increase or decrease in normal load, which will be taken care of by the controller.

A piezoelectric actuator works on the principle of the piezoelectric effect. A voltage applied to a Piezoelectric Transducer (PZT) will result in an almost immediate expansion thereof. This makes the use of piezoelectric materials highly suitable for high dynamic actuation and positioning. A drawback however is that piezoelectric materials experience hysteresis and creep, requiring a controller to ensure accurate positioning. A feedforward combined with a feedback controller to calibrate the hysteresis would work to ensure accurate positioning. On top of that, a very stiff frame should be put behind the piezo actuator to make sure the entire setup will not start vibrating over time.

3.1.3 Sensing

The sensors in the setup serve the following purposes:

- Measure friction at the contact
- Measure position of the spherical specimen.
- Measure relative displacement between the flat specimen and the spherical specimen
- Measure position of the flat specimen.
- Measure the normal load at the contact.

If possible, no-contact sensors are preferred as they will not interfere with the measurement. The friction at the contact is measured using a force transducer. More on that later. The relative displacement between the flat specimen and the spherical specimen is measured using two position sensors. There are a number of position sensors that could facilitate measurement of the relative displacement of the contact and the position of the flat specimen. Inductive sensors, capacitive sensors, laser interferometers and optical encoders are examples of linear no-contact sensors.

Inductive sensors generally have a resolution that is too low for the requirements. Capacitive sensors have a resolution and accuracy that is high enough, but a relatively low sampling frequency and short measuring range. Laser interferometers could fit all requirements, but are very expensive, especially considering the fact that two would be needed to fullfil the position sensing needs. Optical encoders represent the best trade-off between performance and cost.

Position of flat specimen The position of the flat spherical specimen is measured with a linear optical encoder. The placement of the optical center, the center of the readhead of the optical encoder, is important. Ideally, one would place the position sensor in-plane with the contact to minimize what is called Abbe offset and Abbe error.

Relative displacement at the contact The relative displacement between the contact is measured by measuring the absolute displacement of the spherical specimen and the flat specimen. This is done using two optical encoders. Ideally, the position of both the spherical specimen and the flat specimen are measured in-plane with the line of action.

Normal load at the contact The normal load exerted on the contact is determined by calculating the current applied on the voice coil actuator combined with measuring the deflection of the flexure used to vertically position the spherical specimen onto the flat lower specimen. Since the current of the voice coil is directly proportional to the force applied, the force applied by the voice coil can be determined that way. Combined with measuring the deflection of the flexure used to position the spherical contact vertically onto the lower flat specimen, the total force applied on the contact is known. The vertical deflection of this flexure is measured using a no-contact optical encoder as it has a high sampling frequency, easy installation and relatively low cost.

3.1.4 Friction measurement

The friction at the contact is measured with a force transducer; a mechanism that converts mechanical stress to a measurable electrical signal. Strain gauges, piezoelectric shear force sensors, capacitive force sensors are options that could be bought off-the-shelf. Considerations regarding measurement interference, budget constraints, and sampling frequency led to the decision to design a custom force transducer. The principle of the in-house force transducer will have a flexure mechanism with a position sensor measuring the flexure deflection. In dynamic operation, one can determine the friction force when the mass, deflection in time and flexure stiffness is known. The required flexure stiffness is based on the required response of the flexure and mass, the resolution of the position sensor used and the required resolution in the force measurement. The required force resolution is based off the lowest measured friction force that should be measured from the requirements. Once a position sensor is chosen with adequate resolution and sampling frequency, the resolution of the position sensor and required force resolution is then used to determine the required flexure stiffness. By Hooke's law, the friction force that is measured is then determined by equation 14. Where F is the friction force, K is the flexure stiffness and δx is the flexure deflection. More on this in section 3.2.3

$$F = K\delta x \tag{14}$$

3.1.5 Mounting frame

Now that the most important components of the system are discussed, a frame is designed to keep everything rigidly in place. The frame must hold the three position sensors used in the setup, together with three flexures and two actuators. A separate frame is designed for the Piezo actuator to partially decouple the forces exerted from the piezo actuator into the whole setup. The frame will serve the purpose of holding twp parts in place while simultaneously providing adequate stiffness for the parts used in the setup. There are a number of geometrical frames that could be used for holding all the necessary equipment together. To name a few, there are O-shaped frames, C-shaped frames, U-shaped frames and H-shaped frames.

A C-shaped frame is chosen for this setup to allow for easy access for the integration of additional components, such as an infrared camera. An O-shaped frame could potentially offer more stiffness, but monolithic machining of this type of frame is complex, which could be solved by machining the frame in more than one piece for the frame. However, this introduces additional components, increasing the risk of misalignment, microslip, and backlash. A C-shaped frame can be constructed of one part. This type of frame leaves three sides open: two for placement of equipment and one for reaching/installing equipment.

In terms of stiffness, it is important to consider the dimensions and the materials chosen to construct this frame to ensure the frame is stiff enough to hold the equipment in place during operation. The frame's natural frequencies must be sufficiently high to avoid interference with measurements.

3.2 System overview

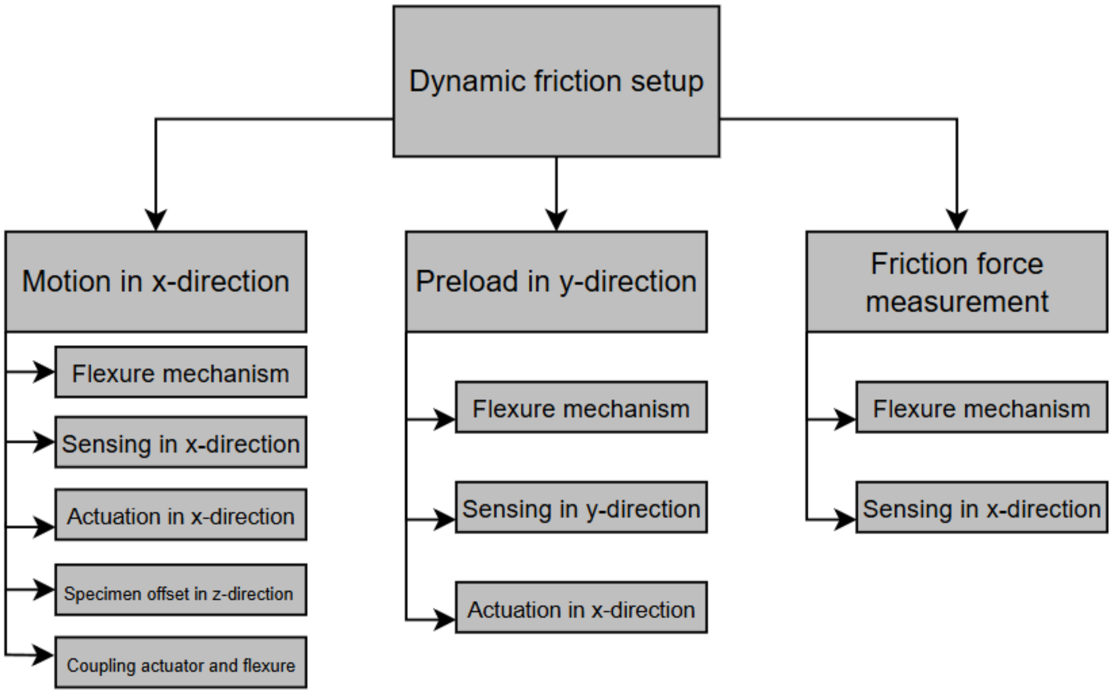

Figure 11: System overview of main components

The decision of two independent 1 DOF mechanisms and a seperate flexure based force transducer, means that three subsystems must be designed to facilitate all requirements of the setup. The system overview in figure 11 shows the most crucial parts of the system. The entire system can be divided into three subsystems, each with its components in terms of flexures, sensing, and actuation. Each of these components is chosen taking into account the requirements that are made for this setup. Along with the produceability, price 10, present errors and ease of use are crucial to determine adequate components for the setup. A conceptual design that resulted from this is the system shown in figure 11. It can be seen that three subsystems have to be designed, each containing their own instrumentation and components.

3.2.1 Subsystem for motion in x-direction

The subsystem that ensures motion in the x-direction, the bottom system, is the part of the setup that holds the lower flat specimen. This specimen is then displaced with straight guidance according to a desired velocity profile. The force required to move the lower specimen will be provided by an actuator, while the straight guidance will be provided by a flexure mechanism. A flexure mechanism is chosen in this system, because it can generate accurate positioning as it has no friction, backlash, hysteresis and stick-slip behaviour. Moreover, since the deflection of a flexure can be determined with Hooke's law, the resulting displacement from the flexure is highly deterministic. This in turn aids the accuracy of the measurement. Figure 12 shows the main components of the subsystem.

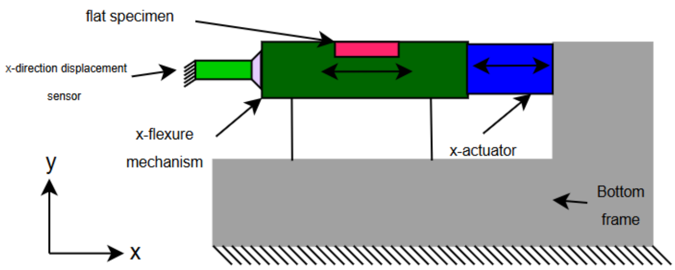

Figure 12: Schematic view of subsystem for motion in x direction

The frame used for this setup serves the purpose of being a semi-rigid body to which the actuator is directly mounted. The aim is to design a frame that is stiff enough to not interfere with the operation of the flexure and actuator. The position sensor that is put in place for the bottom system measures the displacement of the flexure in the x-direction.

Flexure mechanism As stated in Section 3.2.1, a flexure mechanism was selected to provide straight-guided motion in the x-direction. The desired flexure mechanism is a one-degree-of-freedom system, meaning that one degree of freedom is compliant while the remaining five degrees of freedom are stiff.

Several linear and quasi-linear mechanisms were considered like a homogeneous parallel leaf, a double leaf spring, and a triple folded leaf spring mechanism. The objective is to start with a simple design and refine it if complications arise with a particular flexure concept. Another key consideration was to minimize the weight of the flexure mechanism, as it must withstand accelerations of up to 10g. A reinforced parallel leaf spring was chosen that offers high support stiffness and a superior stiffness-to-weight ratio compared to a standard parallel leaf spring. Figure 13 shows a schematic of a standard reinforced parallel leaf spring. Here, L is the total length of the flexure, p is the ratio between the stiff and compliant part of the flexure, E is the Young's modulus of the material used, F is the force applied by a given actuator in the compliant direction, θ and M are respectively the Rotation and moment resulting from this and I is the second moment of area of the compliant part of the flexure expressed in equation 18. If the reinforcement factor p is set to $\frac{5}{6}$, with the ratio between $EI_{reinforced}$ and $EI_{uniform}$ higher than 20, the reinforced section can be assumed rigid because the deflection of the reinforced. As mentioned in the requirements, it was desired that the flexures should endure up to 10 years and the flexure for the x-direction should be able to make a stroke of $200\mu m$ one way.

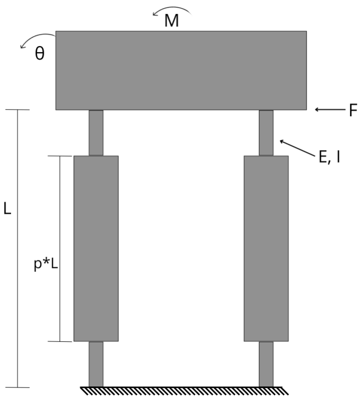

Figure 13: Schematic view of reinforced parallel leaf spring

Once the stress limit at this amount of cycles is estimated, equation 15 is rewritten, such that the required ratio in dimensions does not exceed the fatigue stress limit at maximum deflection. The rewritten equation is expressed in equation 16.

$$\sigma_{b,max} = \frac{3Et\delta x}{L^2} \frac{1}{1-p^3} \tag{15}$$

$$\frac{t}{L^2} = \frac{\sigma_{b,max}(1-p^3)}{3E\delta x} \tag{16}$$

Here, $\sigma_{b,max}$ is the maximum bending stress in the flexure in Pa, E is the modulus of elasticity of the material in GPa, t is the flexure thickness in m, δx is the flexure deflection in m, L is the uniform flexure length in m, and p is the fraction of the flexure which is reinforced, the reinforcement factor. Note that for dynamic operation, the maximum allowed bending stress is equal to the fatigue stress at the required amount of cycles.

On top of this, the critical buckling load should be managed such that the critical buckling load is considerably higher than the normal load applied on the flexure. Equation 17 gives the expression for the critical buckling load. Although buckling starts in the elastic regime, and thus is not an immediate failure mechanism leading to fracture, elastic buckling during operation would mean a diminishment of the accuracy in the system as parasitic motion is introduced as a result. For that reason, the critical buckling load must be considerably higher than the total load applied in the direction buckling can occur.

$$F_{buckle} = \frac{4\pi EI}{L^2}(\frac{1}{1-p})^2 \tag{17}$$

Here, I is expressed as

$$I = \frac{bt^3}{12} \tag{18}$$

Where b is the flexure width and t the flexure thickness. While iteratively determining the optimal dimensions to comply with the maximum allowable stress, and not exceeding the critical buckling load, the objective is to maximize the stiffness of the non-compliant degrees of freedom while maintaining high compliance in the x-direction while also keeping the weight of the flexure low. The stiffness of the reinforced parallel leaf in the x-direction and y-direction are expressed as C_x and C_y respectively in equations 19 and 20.

$$C_x = 12\frac{EI}{L^3}\frac{1}{1-p^3} \tag{19}$$

$$C_y = \frac{EA}{(1-p)(1+\frac{1}{1-p}\frac{12}{B}(\frac{\delta x}{t})^2)} \tag{20}$$

Here, A is the flexure width b times the flexure thickness t and B is expressed in equation 21.

$$B = 700 \frac{(1+q)(1+3q+3q^2)^3}{1+10q+45q^2+105q^3+105q^4} \tag{21}$$

The expression for q is expressed in equation 22

$$q = \frac{p}{1-p} \tag{22}$$

A minimum stiffness ratio of four orders of magnitude between the non-compliant and compliant directions is sufficient to prevent parasitic frequencies from interfering with operation. This ratio ensures that the parasitic eigenmodes are approximately 100 Hz higher than the compliant modes, as estimated using equation 23 as follows.

$$f_n = \frac{1}{2\pi}\sqrt{\frac{k_n}{m}} = \frac{1}{2\pi}\sqrt{\frac{10000k_n}{m}} = \frac{100}{2\pi}\sqrt{\frac{k_n}{m}} \tag{23}$$

Here, f_n is the flexure natural frequency in direction n, expressed in Hertz, k_n is the flexure stiffness in direction n, expressed in N/m, and m is the flexure mass in kg.

Lastly, parasitic motion of the flexure is something important to keep into account for keeping the error in position small. Parasitic motion can occur in shortening or rotation. For a stiffened parallel leaf, the shortening is calculated by equation 24[18].

$$\delta y_{shortening} = -0.5 \frac{\delta x^2}{L(1-(1-p))} \tag{24}$$

Here, $\delta y_{shortening}$ is the deflection in y as a result of deflection in the x-direction, δ_x is the deflection of the flexure in the x-direction, L is the homogeneous length of the flexure and p is the reinforcement factor. Since the required amount of travel of the flexure is determined by the requirements, the only parameter that can decrease the amount of shortening, is increasing the flexure length. Rotation as a result of deflection in the x-direction is another form of parasitic motion that can occur in the system. This rotation θ in radians was derived by equation 25

$$\theta = \frac{F(L(1-p))^2 - 2Fa(L-p))}{E(Ad^2+4I)} \tag{25}$$

Here, F is the force applied in the x-direction by the actuator, L is the homogeneous flexure length, a is the distance between the point where the force is applied and the bottom of the flexure body and d is the distance between the two flexures of the parallel leaf spring.

Once the optimal dimensions are determined —ensuring compliance with stress, buckling, shortening and parasitic rotation- it is crucial to analyze the natural frequencies of the flexures. These frequencies must be considered to prevent resonance during operation, as excitation of a natural frequency could significantly degrade the system's performance and accuracy. The objective should be to maximize the natural frequencies of the system. A first estimate for the natural frequency f_e of the flexure in the compliant direction is given by equation 26. This is further worked out in section 4.4.

$$f_e = \frac{1}{2\pi}\frac{\sqrt{24EI}}{\sqrt{mL^3}} \tag{26}$$

The remaining natural frequencies in the flexure can be approximated with equation 27. Here, k_n is the flexure stiffness in the direction of interest, and m is the mass that is being moved.

$$f_n = \frac{1}{2\pi}\sqrt{\frac{k_n}{m}} \tag{27}$$

A more in-depth description and analysis on the present eigenfrequencies is discussed in section 4.4.

Actuator Various options have been considered in terms of the actuation in the x-direction. The best choice of actuator is the one that is able to satisfy all requirements, while considering the given budget 10. The requirements relevant to the actuator are

- Delivering between 0.5 and up to 10g of acceleration to the bottom horizontal mechanism.
- Position accuracy of 1% of the distance travelled.

  For the first requirement it is important to consider the force an actuator can deliver over time. The second requirement should be about the errors in both the actuator and the system. Naturally, if the inaccuracies present in the actuator already exceeds the specification of accuracy, that makes the actuator immediately unsuitable.

Many off the shelf options are often not able to deliver the required stroke at the required maximum acceleration of 10g. Two options that arose that are in essence able to satisfy the requirements are an amplified piezo actuator and a voice coil.

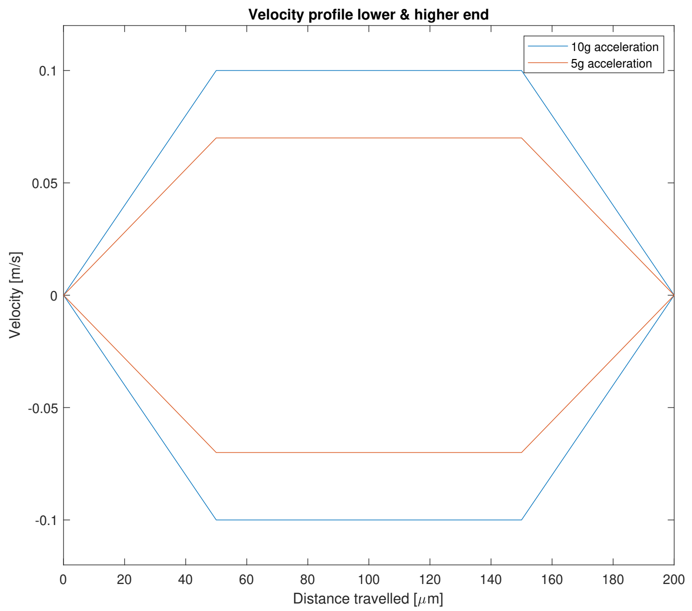

Figure 14: Recirpocating velocity profile

See figure 14. Based on this velocity profile, together with the mass of the parts and the stiffness of the flexures, an initial estimation of the force required to move the horizontal flexural system can be determined. The necessary equations for this estimation is listed as:

$$\begin{aligned} F_{x,required} &= F_{flexure} + F_{inertia} + F_{friction} \\ F_{flexure} &= C_x \delta x \\ F_{inertia} &= M_{tot} a \\ F_{friction} &= \mu_d F_n \end{aligned} \tag{28}$$

C_x is the flexure stiffness in the x-direction, δx is the flexure deflection in the x-direction, M_{tot} is the total mass being moved, a the time dependent acceleration, μ_d is the dynamic friction coefficient and F_n is the applied normal load on the spherical specimen. Although two out of three of the contributing forces are known, system errors and dynamic friction at the contact surfaces remain uncertain. Therefore, an error analysis will be conducted to quantify the existing errors in the system, and a separate subsystem will be designed to measure the dynamic friction during operation.

After identifying the forces contributing to the force balance in the x-direction and determining the necessary constants, a force-required profile can be established. This profile serves as a first estimate for the actuator output in the x-direction, which drives the horizontal mechanism. It is likely that the desired motion will not be achieved immediately. In that case, feedback control or adjustments to the feedforward signal can be considered to refine the system's performance. Using a piezo actuator, it should not be necessary to use feedback control. A repetitive output should be achieved once the required force is found to move the lower flat specimen with the desired velocity over time.

A piezo stack actuator in itself is capable of delivering very high forces in a short amount of time. A drawback is the fact that stand alone piezo stacked actuators have a very low displacement. An amplifier in the form of a flexure extends the range the piezo stack can deliver, while decreasing the peak force it can deliver at the end effector. Hysteresis and creep are two non-linear phenomena that must be considered when modelling a piezo actuator. If modelled correctly, the behaviour of an amplified stacked piezo actuator can be predicted such that it can be force controlled without the help of feedback control.
Since the flexure is not perfectly straight-guided, directly bolting it onto the piezo actuator would introduce additional stress. To mitigate this, an intermediary component should be placed between the horizontal flexure mechanism and the actuator. A wire flexure is a suitable option, as it provides high stiffness in the length direction while remaining compliant in the deflecting degrees of freedom.

Applying a high force within a short period requires not only a precise understanding of the force requirements and actuator accuracy but also careful consideration of parasitic vibrations during operation. The simplest way to address these vibrations is to use a highly rigid frame that keeps the non-actuating side of the actuator fixed. Although perfect rigidity is unattainable, if the frame's deflection remains negligibly small compared to the flexure deflections, this error can be incorporated into the overall error budget and managed accordingly.

Sensing For sensing in the x-direction, according to the requirements, it should be able to measure $200\mu m$ one way with at least 1% accuracy. The initial thought was to use a capacitive single electrode sensor. It was assumed that a no contact position sensor would be favourable, since an in-contact position would interfere with the measurement and degrade over time. However, there was no capacitive sensor available with a high enough measuring range to be used as the highest range a single electrode capacitive sensor would be able to measure was $100\mu m$. An inductive position sensor was considered, but it was quickly found that its resolution and accuracy were far below requirement. A resolution of $4\mu m$ and sampling rate of 10kHz would be common for inductive position sensors. For that reason, the choice fell on a linear optical encoder from Heidenhain[19].

Remaining components

Lower specimen holder The lower specimen holder is connected to the system moving in the x-direction. The holder should keep the flat bottom specimen in place. In addition, a mechanism must be designed to offset the lower specimen in the z-direction to create new tracks for the bead to slide over.

Actuator frame In case a piezo stack actuator is used, a very stiff frame should be designed. Either the frame should be so stiff that it does not vibrate in a significant manner, or some form of damping should be imposed to counteract internal vibration induced by the actuator.

Wire flexure Since the parallel leaf springs shorten, the connection between the actuators for both systems should be designed such that the direction of shortening is relieved to prevent exessive stress build up. Placing a wire flexure between the actuator and the flexure is a solution for this. The governing equations for a wire flexure stiffness in the x- and z-direction, given as respectively $C_{x,w}$ and $C_{z,w}$, is expressed in equation 29 and 30. Here, E is the Young's modulus, L_w is the wire flexure length, D is the diameter of the wire flexure. It is important to make the wire flexure compliant relative to the shortening direction of the horizontal flexure such that internal stress is relieved.

$$C_{x,w} = \frac{E(\frac{\pi}{4})d^2}{L_w} \tag{29}$$

$$C_{z,w} = \frac{12EI}{L^3} \tag{30}$$

Just like with the horizontal flexure, it holds for the wire flexure that the maximum allowed bending stress should not exceed the fatigue stress at the required amount of cycles. The bending stress $\sigma_{b,w}$ for a wire flexure is expressed in equation 31.

$$\sigma_{b,w} = \frac{3Edz}{L_w^2} \tag{31}$$

The force exerted by the actuator in the x-direction should not exceed the critical buckling load $F_{b,w}$, expressed in equation 32. The results for the wire flexure are expressed in table 1.

$$F_{b,w} = \frac{4\pi 2EI_w}{L^2} \tag{32}$$

Actuator frame Since a piezo actuator is used, there a need for a stiff frame for mounting and vibration isolation. Ideally, a stiff frame would be designed that is sufficiently stuff such that no resonance occurs from the actuation from the amplified piezo actuator. On top of that, the deflection of the frame should be taken into consideration when deciding what the required stroke is for the actuator. This then becomes the sum of the deflection of the frame including the required stroke made by the flexure in the x-direction.

3.2.2 Subsystem for preload in y-direction

The subsystem for preload in the y-direction delivers the normal load at the contact from above, while also allowing enough flexure deflection to be able to interchange different specimen without interfering with the alignment of the setup. A schematic overview of the subsystem is shown in figure 15.

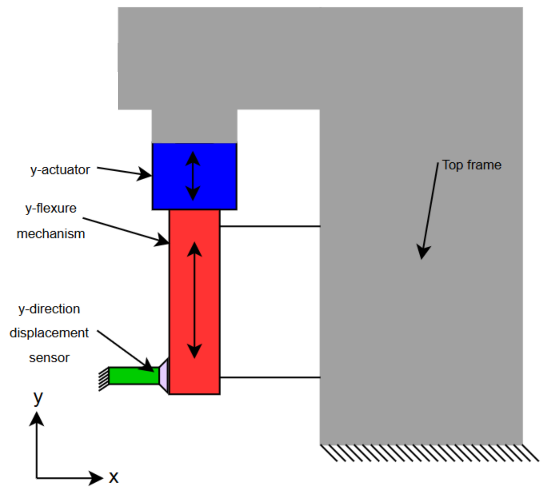

Figure 15: Schematic overview of subsystem for preload in the y-direction

flexure mechanism and actuation As mentioned, a voice coil linear actuator is used to deliver the required normal load a the contact. A reinforced parallel leaf spring is used to allow for motion in the y-direction, and an optical encoder is used to measure the deflection of the flexure.

Normal load measurement The normal load must be measured to be able to maintain a constant desired pressure at the contact. The normal load is delivered by the voice coil. The total force applied at the contact will be determined by measuring the deflection of the flexure in the y-direction and the current running through the voice coil. In an idealized, quasi-static situation, The force delivered by the voice coil is defined by equation 33.

$$F = B \cdot I \cdot L = k_f \cdot I \tag{33}$$

Where F is the Lorenz force delivered by the voice coil, B the magnetic flux density, I the current delivered to the voice coil, L the coil length and k_f the motor constant of the used voice coil. Note that in a dynamic situation, the force balance is different as the magnetic field induced is changing in time. The normal load at the contact is measured by reading the current applied to the voice coil and calculating the spring force. The spring force is calculated the same way as the force transducer. More on actuation of the voice coil in section 4.2.2.

3.2.3 Force transducer

.

The in-house design is a stiffened parallel leaf flexure combined with a displacement sensor. Several off the shelf sensing options were considered, they either had to be in physical contact, were too large to be placed close to the line of action of the contact, the sampling rate was not high enough or the resolution was not high enough. For that reason, a friction force sensor is designed in-house. This in-house design consists of a flexure combined with a position sensor. If one knows the stiffness and deflection of the flexure and the mass that is being moved, The force measured by the sensor $F_{friction}$ is defined by equation 34.

$$F_{friction} = M_{ff} \frac{\delta^2 x}{\delta t^2} + k_{ff} x(t) \tag{34}$$

Here, M_{ff} is the moving mass of the flexure, $\frac{\delta^2 x}{\delta t^2}$ the acceleration of the mass, k_{ff} the flexure stiffness and $x(t)$ is the position of the mass. The position will be measured by a linear optical encoder which measures position over time, so the acceleration can be found by numerical differentiation.

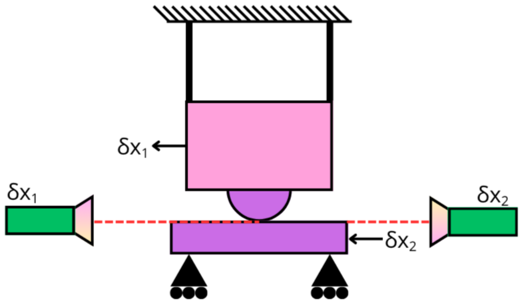

Figure 16: Force transducer for measuring friction at the contact

Figure 16 shows a schematic of the force transducer consisting of a flexure and a position sensor measuring its deflection. In purple, the spherical and flat specimen are seen. At the top, the flexural part of the force transducer is depicted as a pink moving mass holding the spherical specimen, with flexures connected to it. At the bottom in green, the position sensor measuring the displacement of the spherical specimen is placed, along with the position sensor that measures the displacement of the flat specimen. Note that the flat specimen is allowed to slide horizontally. Note that the δx_2 position sensor used in

As mentioned earlier, the force sensor must measure a friction force between 0.1mN and 7N. The lower end specification determines the required resolution. A flexure is used with a position sensor to measure the force, which means that the deflection of the flexure should be measurable by the position sensor that is chosen.

The response time should stay within 5% of the maximum measuring time t_{min} of the mass spring system, meaning the response time should not exceed 74,6 μs. Keeping the weight M_{ff} of the flexure under 10 gr, the required minimum stiffness k_{ff} must be 3.592 $N/\mu m$ using equation 35 and ζ equal to zero as this would give the slowest response with a value for ζ between 0 and 1.

The response time T_r of one oscillation of the mass spring part of the friction force sensor is defined in equation 35.

$$T_r = \frac{2\pi}{\omega_0\sqrt{1-\zeta^2}} \tag{35}$$

Where ω_0 is the undamped natural frequency of the mass-spring system, defined by equation 36

$$\omega_0 = \sqrt{\frac{k_{ff}}{M_{ff}}} \tag{36}$$

Sensor choice The displacement sensor that is to be chosen must have a

Placement The in-house force sensor will be connected in series with the system for pre-load of the specimen in the y-direction holding the spherical specimen. The compliant direction of the flexure will be in the x-direction. See figure 26 and 27 for reference.

Another important aspect to consider in the placement of the sensor components is the Abbe error, the error that exists due to a combined rotational and linear offset. The abbe error ϵ is defined in equation 37.

$$\epsilon = hsin\theta \tag{37}$$

Here, h is the offset between the measuring point and the to be measured point, θ is the angle of rotation. A schematic is shown in figure 34. The angle of rotation θ for a stiffened parallel leaf spring is defined by equation 25. To minimize the Abbe error, either the angle of rotation or the Abbe offset must be minimized. The angle of rotation can be minimized, but the Abbe offset can be set to zero, placing the displacement sensor in-plane with the line of travel of the spherical specimen effectively mitigating the effect of the Abbe error. See figure 26 for clarity.

4 Proposed solution

This chapter discusses the final concept able to solve the problem that is to be solved. A complete setup is proposed where every aspect is worked out in further detail from the conceptual design in chapter 3. The complete 3d design is shown in figure 17

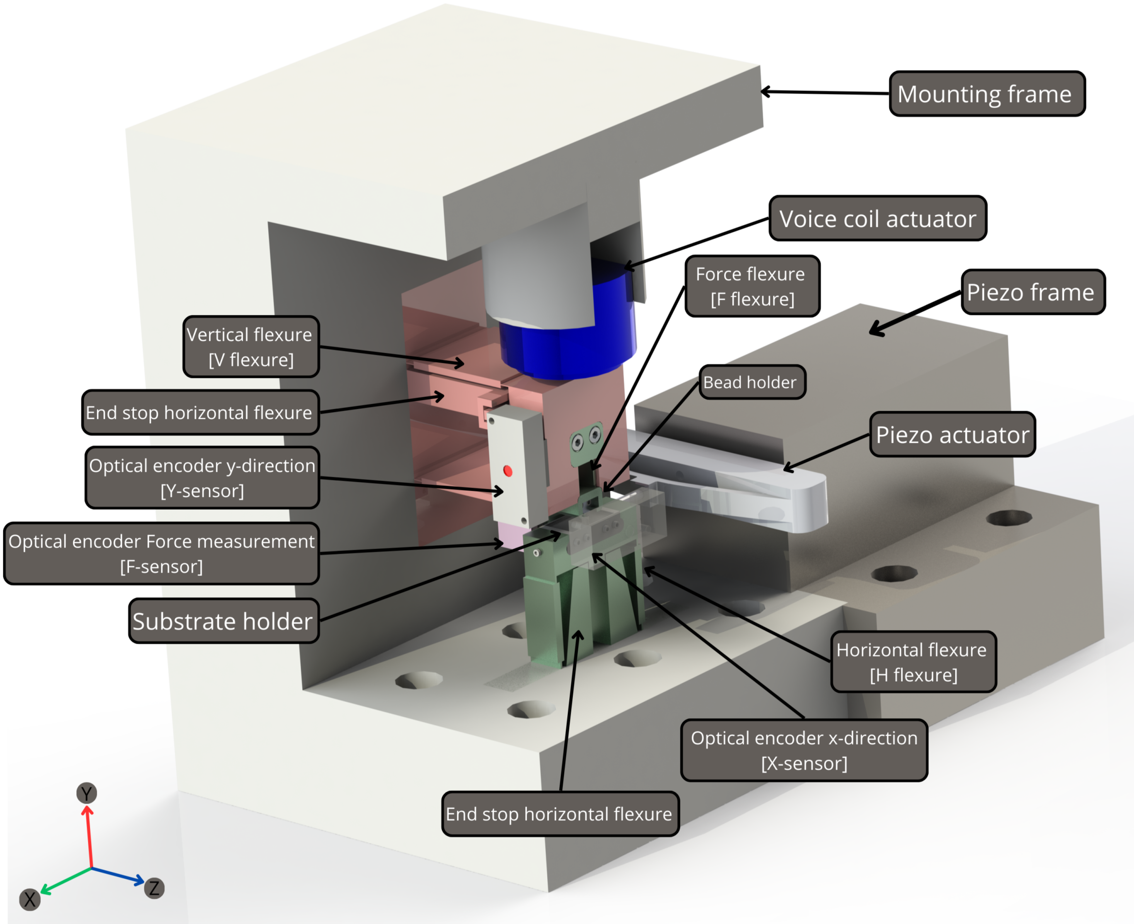

Figure 17: Complete overview of proposed dynamic friction setup

4.1 Horizontal mechanism

The horizontal mechanism facilitates the tangential force required to accelerate the lower flat specimen. A optical encoder is used to measure the flexure deflection, and a mounting mechanism is put in place to tighten and move the lower flat specimen over the z-axis. Figure 18 shows the final result.

4.1.1 Flexure mechanism

The material, chosen for manufacturing the flexures used in the system, was based on several factors. It must have a high fatigue life and low weight. This means that a low-density, high-strength material is favourable in the selection process. Making use of Granta Edupack, the options narrowed down to steel, aluminium alloy, magnesium alloy and CFRP. Since CFRP is a non-homogeneous material, this makes predicting the failure behaviour over time extremely difficult. For that reason, stainless steel was initially chosen for its high strength, but was replaced with 7075 T6 aluminium due to the alloy being superior in terms of strength to weight ratio 36. Once the right material is chosen, the fatigue stress limit can be found. Figure 35 shows the SN curve of 7075 T6 aluminium alloy. It is found that the stress limit at 10^7 cycles is 150MPa. This thus means that the maximum stress in the material must not exceed this value.

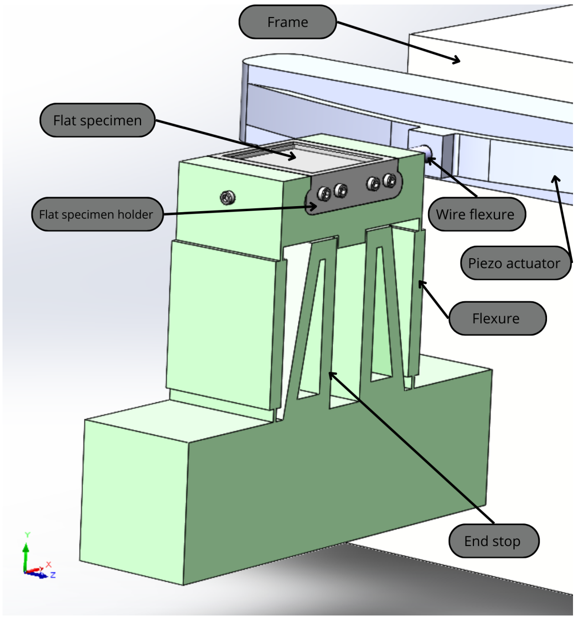

Figure 18: Horizontal mechanism

Following the methodology mentioned in section 3.2.1, The following results were finalized. The most important parameters are expressed in table 1.

Property	**H flexure**	**Wire flexure**
Length [L]	0.04 m	0.04 m
Width [b]	0.015 m	0.002 m (diameter)
Young's modulus [E]	72 GPa	72GPa
Thickness [t]	0.001 m	N/A
Maximum travel []	250 μm	Shortening of H flexure
Fatigue stress limit	150 MPa	150 MPa
Reinforcement factor [p]	0.85	N/A
Bending stress [σ_b]	69.971 MPa	0.324 MPa
Critical buckling load	62.832 KN	0.201 MN
C_y	36 $N/\mu m$	0.168 $N/\mu m$
C_x	1.7493 $N/\mu m$	16.965 $N/\mu m$
C_{rz}	3.2992 nr	N/A
C_z	15.7e $N/\mu m$	0.168 $N/\mu m$
Shortening	0.588 μm	N/A

Table 1: Relevant parameters of wire flexure

After the right dimensions are found, it is important to have a look at the natural frequencies that can be excited within the flexures. A good starting point is to make an analytical estimate of the natural frequencies using equation 26 and 27. Some results of which are shown in table 1 as well. Once the analytical estimates are made, it is important to verify these estimates in a way. It was chosen to do this through FEM.

Verifying the designed flexures' performance is done through FEM in a number of ways. First, the analytical solutions for the flexure stiffness are verified through FEM. Through Hooke's law, the analytical solution of the stiffened leaf flexure of the x-direction is derived. From there, the geometry file of the flexure is imported in the FEM program. A simple static bend-displacement test was put in place to calibrate the stiffness of the flexure. The aim was to stay within 10% deviation of the analytical solution. A Force of 10 N was placed on the flexure and the resulting deflection would then be plotted. See figure 19 for reference. It was evident that the used choice of elements, element type and integration method resulted in either shear locking or hourglassing [20]. These are phenomena where, respectively, the elements are too stiff or too flexible. The solution lies in using fully integrated, hexahedral elements. At the expense of computation time, this yielded a result within 5% accuracy compared to Hooke's law. Figure 19 shows a visual representation of the analysis.

After the stiffness calibration is done, a modal analysis can be done to find which modes of the flexures will be excited at which frequencies. A modal analysis yielded the first four natural frequencies of the flexure which are shown in table 4.

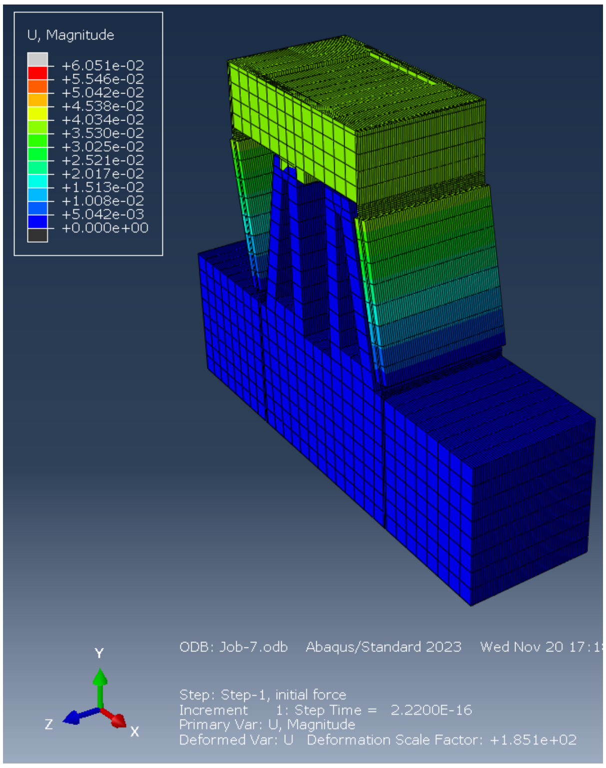

Figure 19: Deflection of the calibrated bottom flexure [mm]

4.1.2 Actuator

Expanding on figure 14, the equations of motion have to be established to solve for the fore required to move the horizontal flexure in the desired. As was discussed, the lower flat specimen must accelerate over a given distance, slide at constant velocity and then slide with a constant deceleration before coming to a short standstill and repeating the same sequence backwards. This is what one reciprocal cycle looks like. However, because it is essentially mass that is moved, a moving object cannot instantly shift from a certain acceleration to zero acceleration. There is a transition region. To account for the transition from one acceleration to another, an amount of jerk must be introduced. Solving the force balance required to detemine the force delivered from the actuator to the flat lower specimen, the equations of motion first have to be solved. This starts with the desired acceleration phases with added jerk in between. This is shown in figure, 23a. From here, numerical integration is used to determine the velocity profile resulting from this, shown in figure 23b. Using numerical integration once more gives the position profile, shown in figure 23c. Having solved for the equations of motion, the force balance described in 28 can be solved. Since the degree of friction is unknown, a constant dummy friction is inserted. The resulting total force required to move the flat lower specimen is plotted in figure 21. Figure 20 Shows the normalized contributing forces.

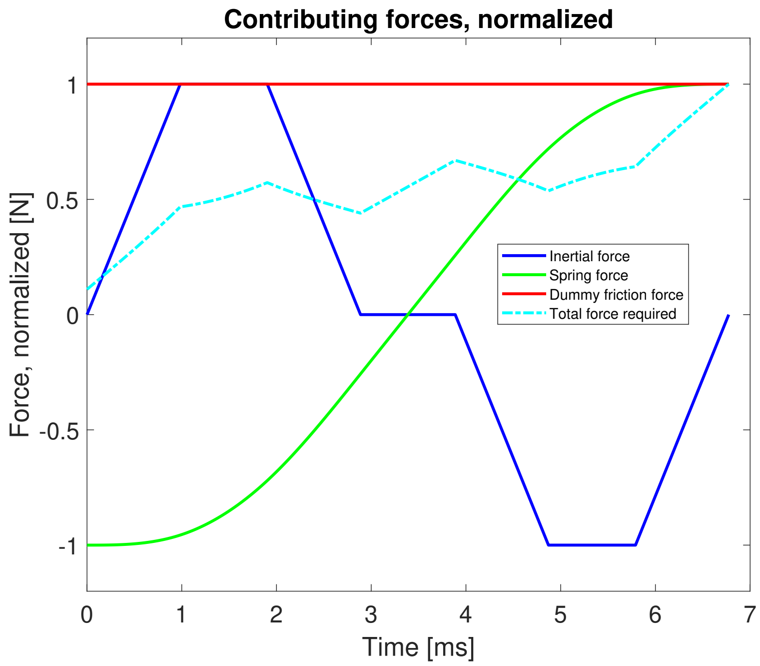

Figure 20: Force required profile

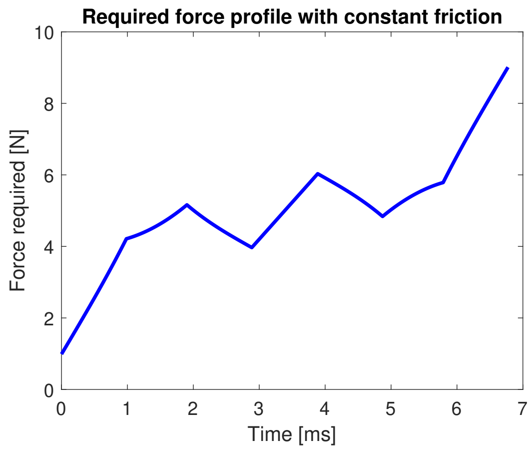

Figure 21: Required force to move the lower flat specimen

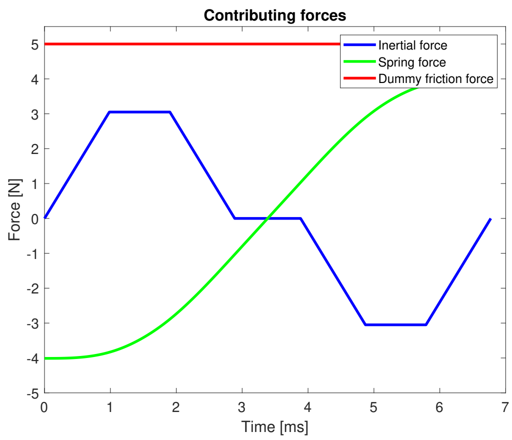

Figure 22: Contributing forces at the lower flat specimen

The jerk is computed to check if there is no infinite jerk. This is done by taking the time derivative of the sum of contributing forces. The following relation is determined in equation 38.

$$\frac{\delta F}{\delta t} = m \cdot \frac{\delta a}{\delta t} = m \cdot \frac{\delta^3 x}{\delta t^3} = m \cdot j \tag{38}$$

Rewriting to find the jerk yields

$$j = \frac{1}{m} \frac{\delta F}{\delta t} \tag{39}$$

The result is plotted in figure 23d. It is shown that there is no infinite jerk.

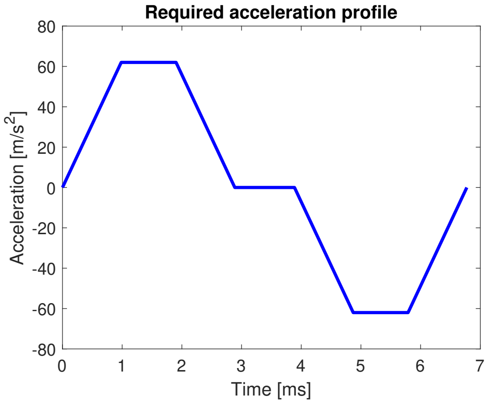

(a) Required acceleration over time

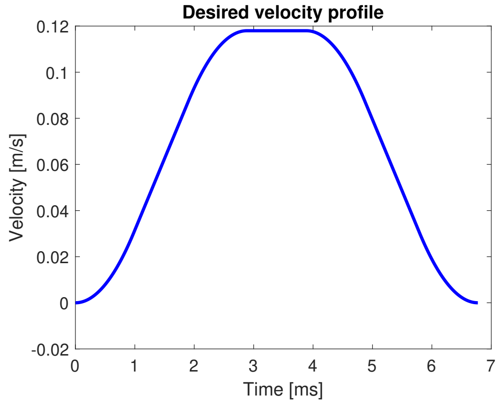

(b) Desired velocity profile over time

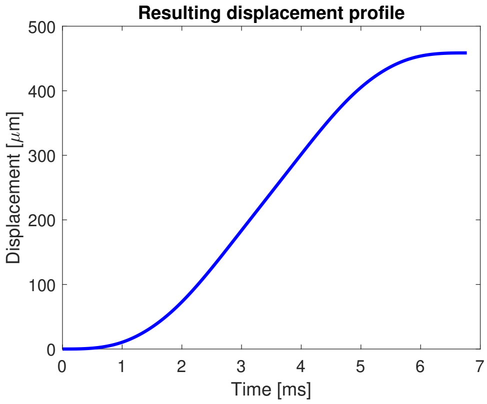

(c) Resulting displacement over time

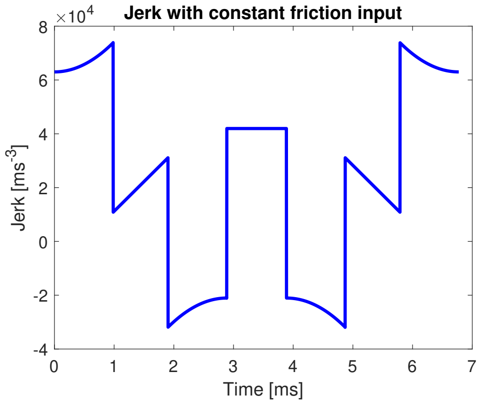

(d) Jerk profile resulting from contributing forces

Figure 23: Plotted equations of motion

The required force profile that the actuator must deliver to the lower flat specimen is found after solving the force balance given using equation 28 and figure 23. The actuator chosen for this setup is the APA500L from Cedrat Technologies [21]. It has a stiffness of 1.1 $N/\mu m$, can deliver a constant force of 1000N, and has a resolution of 29nm in position, translating to a resolution of 0.319 mN in the force. From the force balance in figure 21, the necessary current and voltage can be derived for the APA to move the horizontal mechanism. A very simplified version of how voltage and displacement relates with the APA if described in equation 40

$$V(t) = \frac{x(t)}{d_{33}} \tag{40}$$

Here, V(t) is the supplied voltage, x(t) is the displacement, and d_{33} is the piezoelectric strain coefficient derived to be approximately $3\mu m/V$.

The current I(t) required to drive the piezo is given by

$$I(t) = C\frac{\delta V(t)}{\delta t} \tag{41}$$

Where C is the capacitance of the actuator. Rewriting using equation 40 yields equation 42, yielding a direct relation between velocity and supplied current.

$$I(t) = \frac{C}{d_{33}}\frac{\delta x(t)}{\delta t} \tag{42}$$

A VCA can also be used to deliver the tangental force required to move the lower flat specimen. The working principe is described in section 4.2.2, and the results shown in appendix I.

4.1.3 Sensing

The Lida 47 optical encoder is used for the position sensing of the horizontal flexure mechanism. It is able to sample up to 50 kHz with a measuring step of $0.4\mu m$ and interpolation error of 0.9nm. The interpolation error of a linear encoder is a result of interpolating over the received sine signal read by the encoder. The more you interpolate, the lower the interpolation error. Not only are the requirements important, but the placement of the sensor is vital to prevent a large Abbe error from occurring. The Abbe error is defined as

$$\epsilon = hsin\theta \tag{43}$$

Where h is the offset between the measuring point and the to be measured point, θ is the angle of rotation[22]. A schematic is shown in figure 34. The angle of rotation θ for a stiffened parallel leaf spring is defined by equation 25, and the results are shown in table 3. Both the force measurement sensor and the displacement sensor for the horizontal stage are placed such that the optical center is concentric with the bead, meaning that the Abbe offset is zero, and thus the Abbe error is zero.

4.2 Vertical mechanism

The vertical mechanism consists of the force transducer, VCA, flexure coupled to the VCA, optical encoder to measure the flexure deflection and the stiff frame holding everything together. The final design is shown in figure 24.

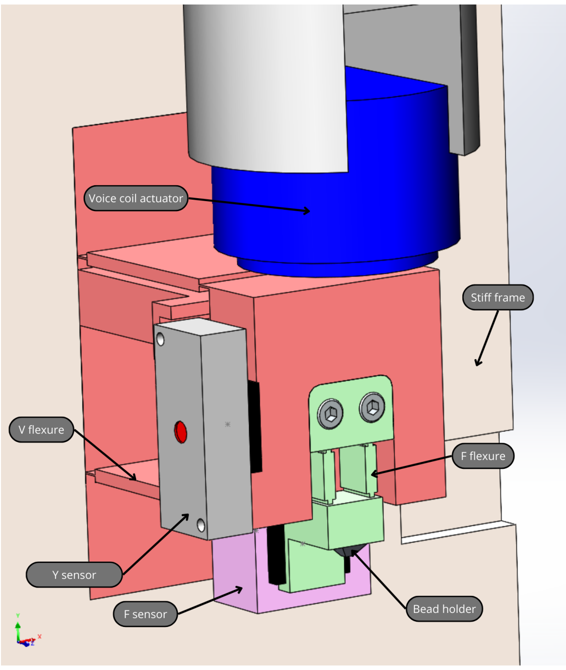

Figure 24: Final design of the vertical mechanism.

4.2.1 Flexure mechanism

The flexure mechanism for allowing normal load at the contact, is also designed to be moved upward up to 2mm to make room for swapping specimen. The flexure stiffness in the compliant direction is tailored such that it will not exceed a maximum bending stress of 150 MPa during its lifetime to ensure a lifetime of 10 years. The result is shown in figure 24

Property	V flexure
Length [L]	0.055 m
Width [b]	0.005 m
Thickness [t]	0.0004 m
Young's modulus [E]	72 GPa
Reinforcement factor [p]	0.85
Maximum deflection	2 mm
Fatigue cycle limit	10^7
Fatigue stress limit [σ_f]	150 MPa
Stiffness in y [C_y]	436.4 N/μm
Stiffness in x [C_x]	0.007178 N/μm
Stiffness in z [C_z]	112.2 N/μm
Rotation [θ]	
Shortening	0.4364 μm
Critical buckling load	3.545 kN
Bending stres [σ_b]	148 MPa

Table 2: Relevant parameters of V flexure

4.2.2 Actuator and sensing

For normal load in the y-direciton, the Voice coil actuator (VCA) used is the NCC03-15-050-2X from H2W tech [23] and the same optical encoder is used to measure position. The coil delivers 22.3 N at 100% duty cycle, 66.8 N at 10% duty cycle, and a nominal stroke of 6.4mm. It was mentioned by equation 33, what the relation is between current and Lorentz force delivered by the VCA. However, in a dynamic situation, the force balance is more complex. The first difference is that the induced magnetic field by the moving current through the coil is not constant, but time dependent. This is defined in equation 44. Here, $k_f(I)$ is the effective force constant dependent on saturation of the magnetic field, k_{f_0}, the force constant given by the manufacturer, I(t) is the current delivered at time t and I_{sat} is the saturation current.

$$k_f(I) = \frac{k_{f_0}}{1 + \left|\frac{I(t)}{I_{\text{sat}}}\right|} \tag{44}$$

The Lorentz force F_l is then defined as

$$F_l = k_f(I) \cdot I(t) \tag{45}$$

The force balance for a VCA in a dynamic situation is defined in equation 46. Here, M is the total moving mass, R the coil resistance, $\frac{k_f^2}{R}$ a damping term resulting from back electromotive force (back EMF) 47, and k the flexure stiffness.

$$F = \frac{k_{f_0} I(t)}{1 + \left|\frac{I(t)}{I_{\text{sat}}}\right|} = M\frac{\delta x^2}{\delta t^2} + \frac{k_f^2}{R}\frac{\delta x}{\delta t} + kx \tag{46}$$

$$\text{EMF} = k_f \cdot v(t) \tag{47}$$

The required current I(t) to achieve the desired normal load at the contact is defined in equation 48.

$$I(t) = \frac{F(t)}{k_f(I)} \tag{48}$$

The required voltage V(t) is defined in equation 49. Here, L_{coil} is the coil inductance given by the manufacturer, R(t) the time and Temperature dependent coil impedance, I(t) the supplied current and EMF the resulting EMF.

$$V(t) = L_{\text{coil}} \frac{dI(t)}{dt} + R(t)I(t) + \text{EMF} \tag{49}$$

The coil will heat up as a result of current flowing through it. This is called Joule heating. The Thermal power dissipated into the coil due to Joule heating is defined in equation 50.

$$P_{Jh}(t) = I(t)^2 R(t) \tag{50}$$

Here, R(t), the temperature-dependent impedance, is defined in equation 51. R_0 is the coil impedance given by the supplier, α the temperature coefficient of copper and T(t) the measured coil temperature.

$$R(t) = R_0 \left[1 + \alpha \left(T(t) - 25\right)\right] \tag{51}$$

It is important to know how much the coil will heat up during operation and the cooling power required in case the coil temperature exceeds safety operation limits. Equation 52 defines the relation between the Joule heating P_{Jh}, and energy dissipation to the ambient environment.

$$C \frac{dT(t)}{dt} = P_{Jh}(t) - hA \left(T(t) - T_0\right) \tag{52}$$

Here, C is the heat capacity of the wire, T(t) is the temperature at time t, $\frac{dT(t)}{dt}$ is the rate of temperature change, $P_{Jh}(t)$ is the power input at time, h is the lumped heat transfer coefficient of free convection and conduction, A is the surface area of the wire and T_0 is the ambient temperature. The result is plotted in figure 25. It can be concluded that the steady state temperature during operation lies around 63 degrees Celcius, and this would take 1.2 Watts of additional heating to keep the coil running at ambient temperature. Even though the temperature rise is well within safety limits of the VCA, it would be beneficial to implore active cooling to keep the coil temperature constant. Doing this would make controlling the normal load much easier, as the required current for delivering the normal load is temperature dependent.

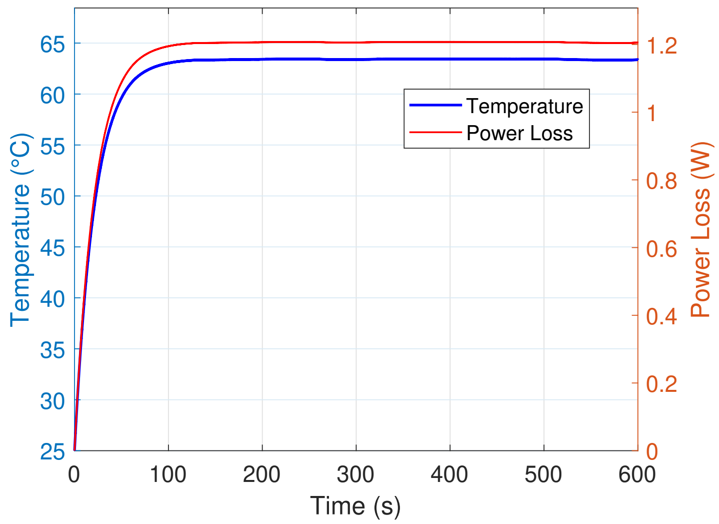

Figure 25: Transient temperature curve of the coil as a result of Joule heating

4.3 Friction force measurement

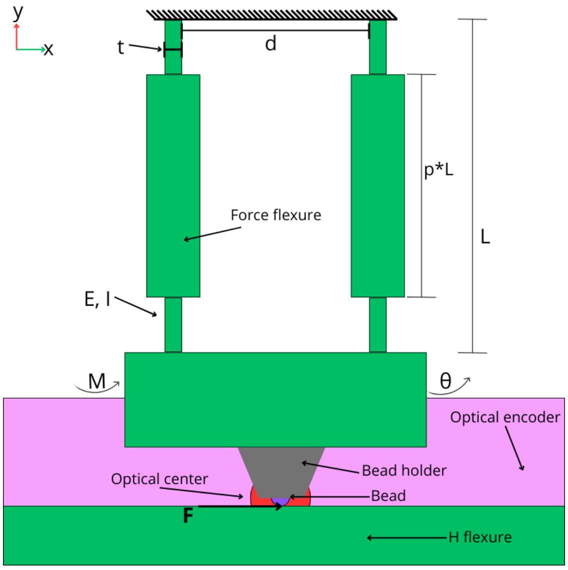

Figure 26: Friction force measurement xy-view

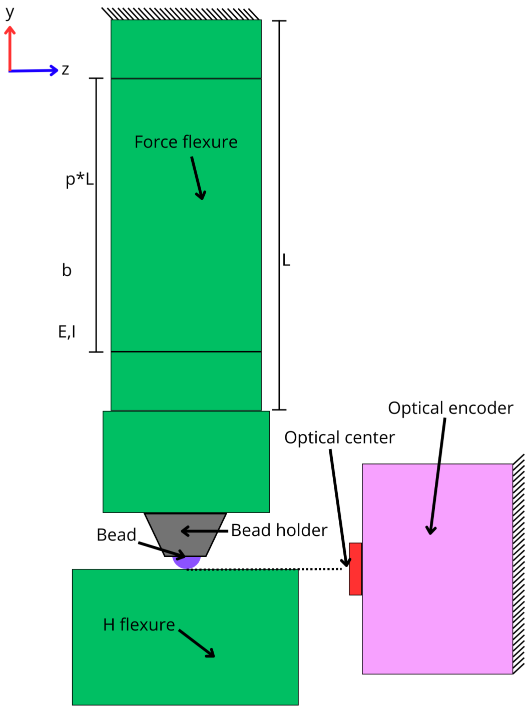

Figure 27: Friction force measurement zy-view

Requirements Looking at the requirements, the normal force delivered to the two specimen varies between 0.1 and 10N. It is expected that the friction coefficient μ_f between the contact will vary between 0.1 and 0.7 [24]. This means that the friction force occuring at the contact will vary between 0.01 and 7N. From the requirements, the friction force sensor must measure the friction force while maintaining an accuracy of 1% over the range of applied loads. This means the sensor should be able to detect between 0.1mN and 10N. Another requirement is that the amount of samples during each phase, be it constant accelerated slip, slip at constant velocity or constant decelerated slip, should at least be 100 samples. The shortest measuring time would be combining the highest acceleration with the shortest slip distance set in the requirements. According to section 2.2, the shortest slip distance s is 27.36 μm, and the highest acceleration a is 10g. Using equation 53, The shortest measurement time t_{min} is determined to be 0.746 ms. Having 100 samples during this measurement time means that the sampling frequency for measuring the friction force f_s must be 134 kHz minimum as per equation 54. The determined dimensions for the flexure part of the force transducer is shown in table 3

$$t_{min} = \sqrt{\frac{2s}{a}} \tag{53}$$

$$f_s = \frac{1}{T} = \frac{100}{t_{min}} \tag{54}$$

Property	Force flexure
Length [L]	0.0127 m
Width [b]	0.008 m
Thickness [t]	0.0013 m
Young's modulus [E]	72 GPa
Reinforcement factor [p]	0.85
Maximum deflection	2.1861 μm
Fatigue cycle limit	10^7
Fatigue stress limit [σ_f]	150 MPa
Stiffness in y [C_y]	393 N/μm
Stiffness in x [C_x]	3.202 N/μm
Stiffness in z [C_z]	10154 N/μm
Rotation at maximum deflection [θ]	0.6439 nrad
Shortening	
Critical buckling load	0.3652 MN
Bending stres [σ_b]	0.8022 MPa

Table 3: Relevant parameters of the force flexure

Choice of sensor To measure the dynamic friction between the spherical bead and the flat contact surface, a suitable sensing method was chosen. The force measurement system operates using a combination of a stiffened leaf flexure and an optical linear encoder. The required measurement accuracy is 1% of the lowest measurable force, which is 0.01 N, meaning the sensor must have a resolution of 1 mN. By analyzing the smallest step size of the employed linear encoder and correlating it with the required force resolution, the necessary stiffness for the flexure was determined. The Heidenhain LIP201 encoder, with a minimal step size of 31.25 pm, dictates that the flexure must have a stiffness of 3.2 $N/\mu m$.

Placement of sensor The placement of the optical encoder is also critical. Ideally, measurements should be taken directly at the point of contact; however, this is not feasible. Therefore, a trade-off was made by positioning the encoder for force-displacement measurement in the bead's zx-plane. This configuration ensures zero offset in this plane when the force flexure moves along the x-direction, effectively minimizing Abbe error in this direction and plane, thereby significantly enhancing the accuracy of the dynamic force measurements.

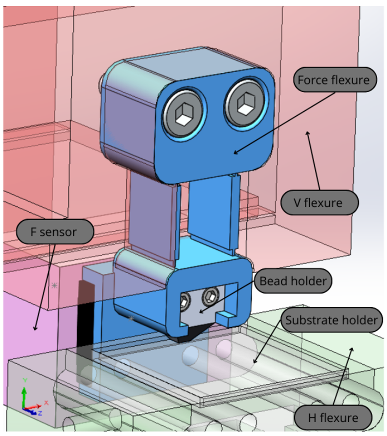

Figure 28: Flexure part of the force measurement system

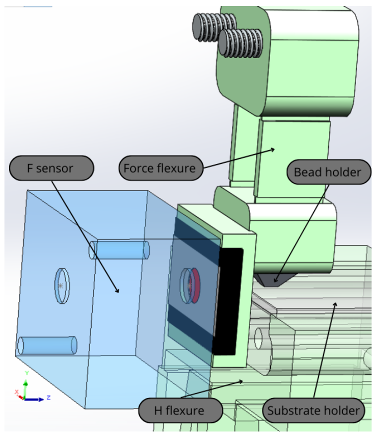

Figure 29: Sensor part of the force measurement system

However, with this configuration, it is not possible to achieve Abbe alignment across all planes. The rotation around the y-axis in the yx-plane is not aligned as there is an Abbe offset of 15.3 mm.

Nonetheless, rotational offsets around the y-axis are not expected as there is no moment acting, provided that the load in the x-direction is centered along the bead's line of motion. The final concept is illustrated in figures 28 and 29.

As shown in Figure 28, the bead holder is directly connected to the force-measuring flexure. During operation, the bead holder may undergo deflection, potentially causing an offset. Therefore, it is crucial to quantify this deflection under various conditions.

Several factors influence the design of a sufficiently rigid holder for the glass bead attached to the vertical mechanism. The holder must provide space for cameras and sensors near the specimen while maintaining adequate stiffness during operation. Figure 30 illustrates the bead holder (grey), which is attached to the force-measuring flexure (green) and subsequently connected to the vertical flexure (red).

To ensure sufficient stiffness, initial estimations were performed using the SolidWorks simulation toolbox. Iterative simulations were conducted to determine the appropriate material and dimensions necessary to limit bead holder deformation within the required accuracy range. The simulation results are shown in Figure 31. A tangential force of 10 N was applied to the narrow end of the holder, with orange arrows indicating the encastre boundary condition, which means all degrees of freedom remain fixed in that region. The simulation revealed a maximum deformation of $0.149\mu m$ in the negative x-direction, which is well within the acceptable accuracy limits.

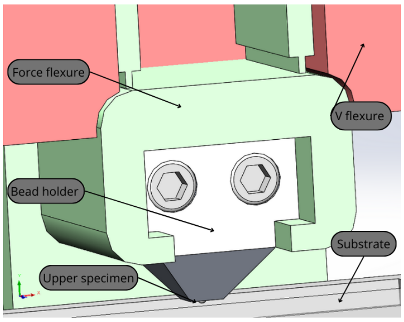

Figure 30: Top specimen holder

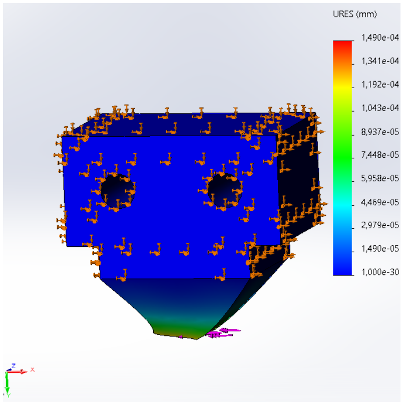

Figure 31: Simulated deflection of the top specimen holder [mm]

4.4 Frequency analysis

After having designed flexures according to the requirements, and having chosen the suitable components in the system, it is important to do a frequency analysis. It is important to know which parasitic frequencies can be present in the system and at which frequencies they occur. If some eigenmodes occur at lower frequencies than expected, the design could be made stiffer or lighter to shift the frequency upward and effectively increase the bandwidth. On top of that, one should have an idea of which of those frequencies can be excited during dynamic operation.

Things that will influence the open-loop frequency response of the system during dynamic operation is

- Input for the actuators
- Friction coefficient between the bead and substrate
- Applied normal load

The frequency analysis will be split into two parts. In the first part, a modal analysis is done on the individual constituent parts of the system. This is done in Abaqus. In the second part, a modal analysis is executed to compute the frequencies that are excited under different operating conditions when everything is assembled.

The first part of the frequency analysis starts with a stiffness calibration of the flexible parts of system. After importing the geometry files of these parts into Abaqus, adequate boundary conditions and element type must be imposed. It is important to be mindful of hourglassing and shear locking. This is a phenomenon where elements are respectively too flexible, or too stiff. To ensure that the flexible elements possess the elastic properties that one would expect, it is important to make an element choice which will ensure expected behaviour [20]. Next, a static analysis is done on the flexure, where a known force is applied in the most compliant direction of the part. Given the stiffness in the direction the force is applied, one can estimate the deflection with Hooke's law, $F_s = -kx$. Where F_s is the spring force that should be overcome, k is the flexural part stiffness and x is the deflection in the direction the force is applied. Comparing this estimation of deflection with the deflection that is computed by the static analysis, says how flexible or stiff the FEM part is compared to an idealized analytical solution. For all parts, a known force of 10 N is applied, for which the deflection is measured. The measured deflection is used together with the applied force to yield the model stiffness of the dedicated part.

The next step is the extraction of eigenmodes. This is done by solving the eigenvalue problem for an undamped oscillation. The eigenvalue problem is expressed in equation 55.

$$(-\omega^2 M^{mn} + K^{mn})\phi^n = 0 \tag{55}$$

Here, ω represents the natural frequency, M is the mass matrix of the dedicated part, K is the stiffness matrix of the dedicated part, ϕ is the eigenvector and m and n represent the degrees of freedom. A Lanczos eigensolver is used to find the eigenmodes [25]. The residual modes are added to the found natural frequencies, as this drastically improves the accuracy of frequency extraction [26]. Next to the modal analysis in FEM, a theoretical approximation is made of the present modes in the system. This is done using equation 26, 27. The results of the first part of the frequency analysis can be found in table 4.

4.4.1 Individual components

Part	f_n FEM	f_n estimate	Stiffness FEM	Stiffness estimate
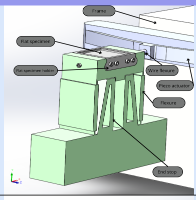	$f_x = 235.7$ Hz $f_z = 2351.2$ Hz $f_{ry} = 4458$ Hz $f_{i1} = 4680$ Hz	$f_x = 212.2$ Hz $f_{ix} = 386.2$ Hz $f_z = 3183$ Hz $f_y = 9627$ Hz	$C_x = 8.32e + 4Nm^{-1}$	$C_x = 8.75e + 4Nm^{-1}$ $C_y = 1.8e + 8Nm^{-1}$ $C_z = 1.97e + 7Nm^{-1}$
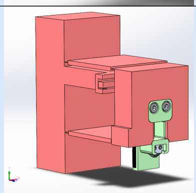	$f_y = 36.21$ Hz $f_x = 1702$ Hz $f_{i1} = 2049$ Hz $f_{i2} = 2120$ Hz	$f_y = 32.95$ Hz $f_{iy} = 59.67$ Hz $f_x = 4118$ Hz $f_z = 5137$ Hz	$C_y = 7.56e + 3Nm^{-1}$	$C_x = 1.75e + 8Nm^{-1}$ $C_y = 7.2e + 3Nm^{-1}$ $C_z = 1.12e + 8Nm^{-1}$
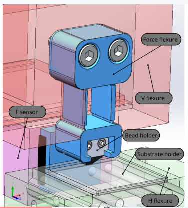	$f_x = 2844$ Hz $f_{i1} = 4202$ Hz $f_{i2} = 7881$ Hz $f_{ry} = 9242$ Hz	$f_{ix} = 428$ Hz $f_x = 3445$ Hz $f_y = 38175$ Hz $f_z = 173550$ Hz	$C_x = 3.68e + 6Nm^{-1}$	$C_x = 4e + 6Nm^{-1}$ $C_y = 4.91e + 8Nm^{-1}$ $C_z = 1.02e + 10Nm^{-1}$
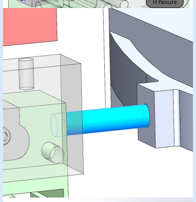	$f_z = 18620$ Hz $f_y = 39933$ Hz $f_{i1} = 66543$ Hz	$f_z = 11265$ Hz $f_y = 31053$ Hz $f_{i1} = 60877$ Hz	$C_x = 6.55e + 7Nm^{-1}$	$C_x = 6.79e + 7Nm^{-1}$ $C_z = 1.68e + 5Nm^{-1}$
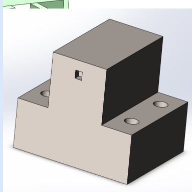	$f_z = 7513$ Hz $f_x = 8807$ Hz $f_{ry} = 9288$ Hz $f_y = 14549$ Hz	$f_z = 4142$ Hz $f_x = 7767$ Hz $f_y = 12108$ Hz	$C_x = 1.72e + 11Nm^{-1}$	$C_x = 1.82e + 11Nm^{-1}$ $C_y = 3.68e + 10Nm^{-1}$ $C_z = 5.17e + 10Nm{-1}$
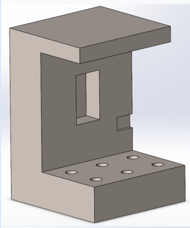	$f_rz = 785.5$ Hz $f_{ry} = 1333$ Hz $f_{rx} = 1732.3$ Hz $f_{ry2} = 1976$ Hz	$f_z = 395.4$ Hz $f_y = 1028$ Hz $f_x = 3652$ Hz	$C_x = 2.91e + 9Nm^{-1}$	$C_x = 2.795e + 9Nm^{-1}$ $C_y = 9.315e + 10Nm^{-1}$ $C_z = 5.17e + 10Nm{-1}$
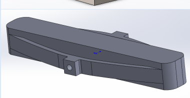	$f_{ry} = 155$ Hz $f_{rz} = 189$ Hz $f_{rx} = 494$ Hz	$f_x = 456$ Hz		$C_x = 1.1e + 6Nm^{-1}$

Table 4: Modal analysis of individual components in the system.

4.4.2 Whole system

Next to the modal analysis of the individual components, a modal analysis is done of the system as well. Table 5, 6, 7 and 8 shows the modes from the FEM model, corroborated with analytical solutions found in literature for comparison. The second part of a dynamic response analysis is done, also in Abaqus. The goal is to see what modes are found when the setup is assembled. This gives insight in the influence different parts have on each other once everything is assembled and the bandwidth that can be achieved using the proposed setup.

FEM	Mode shape	Estimation
31 Hz	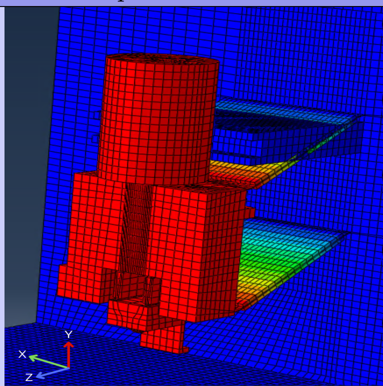	$M = 0.23kg$ $C_y = \frac{24EI}{L^3}\frac{1}{(1-p^3)} = 7.17N/mm$ $f_y = \frac{1}{2\pi}\sqrt{\frac{C_y}{M}} = 28.11Hz$
880 Hz	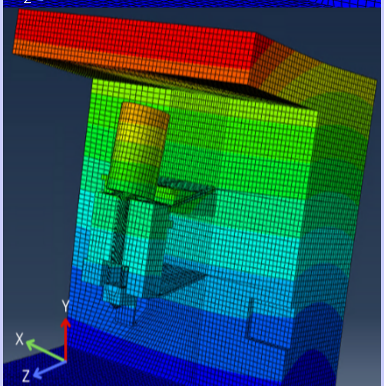	$M = 25.9kg$ $I = Mr^2 = 1.618kgm^2$ $C_{\theta_x} = \frac{GJ}{L} = 75.5Nm/\mu rad$ $f_{rot,x} = \frac{1}{2\pi}\sqrt{\frac{C_{\theta_x}}{I}} = 1087Hz$
1081 Hz	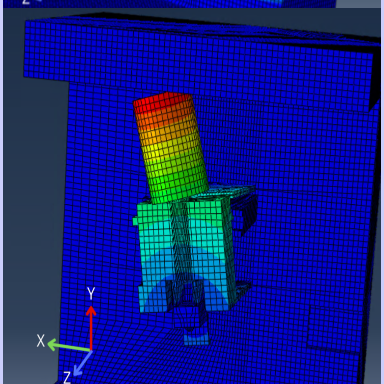	$I = 0.0051kgm^2$ $C_{\theta_z} = \frac{d^2}{2}C_x = 0.212Nm/\mu rad$ $C_x = \frac{1}{2\lambda(4\lambda^2-6\lambda+3)(1-\gamma)+\gamma} \cdot \frac{Eb^3t}{4L^3} = 169.4N/\mu m$ $f_{rot,z} = \frac{1}{2\pi}\sqrt{\frac{C_{\theta_z}}{I}} = 1025Hz$
No displacement	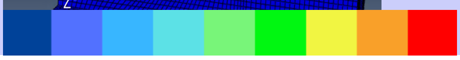	**Maximum displacement**

Table 5: Mode shapes and analytical solutions for upper system

Mode 1 at 31Hz The first mode found in the upper mechanism is modelled as a parallel reinforced leaf spring with a point mass consisting of the shuttle, voice coil magnetic core and the force flexure. A point mass proved to be sufficient and is to be expected since the shuttle, voice coil and force flexure show no deflection in this mode. The stiffness of the vertical flexure is calculated using equation 56, and the eigenfrequency is calculated using equation 57. Here, M is the moving mass.

$$C_y = \frac{24EI}{L^3}\frac{1}{(1-p^3)} \tag{56}$$

$$f_y = \frac{1}{2\pi}\sqrt{\frac{C_y}{M}} \tag{57}$$

Mode 2 at 880Hz The second mode of the upper mechanism was modelled as a torsional spring at the base of the frame with a rotating beam with length L equal to the length of the frame in the y-direction. The equation used to calculate

$$C_{\theta_x} = \frac{GJ}{L} \tag{58}$$

Where J is the torsional constant about the x-axis, defined by

$$J = \frac{bt^3}{3} \tag{59}$$

The eigenmode is calculated using equation 60 which is defined as

$$f_{rot,x} = \frac{1}{2\pi}\sqrt{\frac{C_{\theta_x}}{I}} \tag{60}$$

Where M is the moving mass and I is the rotational moment of inertia of a beam rotating from its base, defined as

$$I = Mr^2 \tag{61}$$

Mode 3 at 1081Hz Assuming small rotations, the rotation over the z-axis of a parallel leaf spring in radians of a parallel leaf spring is defined by

$$u_x = \pm\frac{d}{2}\theta_z \tag{62}$$

Where d is the distance between the two flexures. From Hooke's law it is known that

$$F_y = C_x u_x = C_y\frac{d}{2}\theta_x \tag{63}$$

Where C_x is the flexure stiffness in the x-direction and u_x the deflection in the x-direction. Note that C_x is the shear direction of the vertical flexure. Moving to the moment balance for a single flexure, it says that

$$M_z = \frac{d}{2}F_y = \frac{d^2}{4}C_x\theta_z \tag{64}$$

Where it holds for two flexures that

$$M_{total,z} = 2\frac{d^2}{4}C_x\theta_z = \frac{d^2}{2}C_x\theta_z \tag{65}$$

This yields the following.

$$C_{\theta_z} = \frac{M_{z,total}}{\theta_z} = \frac{d^2}{2}C_x \tag{66}$$

C_x is defined as follows [27].

$$C_x = \frac{1}{2\lambda(4\lambda^2-6\lambda+3)(1-\gamma)+\gamma}\cdot\frac{Eb^3t}{4L^3} \tag{67}$$

Note that the C_x mentioned here equates to C_y for c-shaped deformation on the source page. The rotational stiffness of a reinforced parallel leaf spring over the z-axis is defined as follows.

$$\boxed{C_{\theta_z} = \frac{d^2}{2\left(\lambda(1-\gamma^3)+\gamma^3\right)}\frac{Ebt^3}{12L}} \tag{68}$$

Wherem λ is the length ratio between the flexure part and the reinforced part and γ is the thickness ratio of the flexure part and the reinforced part. The eigenfrequency of this mode is calculated using the following equation.

$$f_{rot,z} = \frac{1}{2\pi}\sqrt{\frac{C_{rot,z}}{I}} \tag{69}$$

Where I is the moment of inertia around the z-axis. Since this is a relatively complex geometry, the moment of inertia was generated from the SolidWorks mass property manager. Before this was done, a simple geometry was used to determine whether Solidworks complies with parallel axis theorem used for determining the second moment of area. This simple derivation can be found in table 11.

FEM	Mode shape	Estimation
1496 Hz	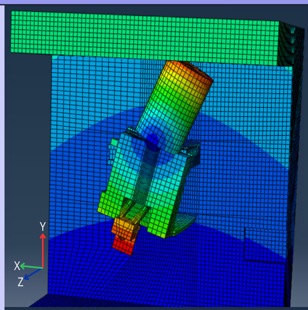	
1712 Hz	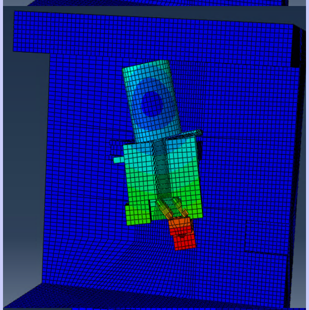	
2025 Hz	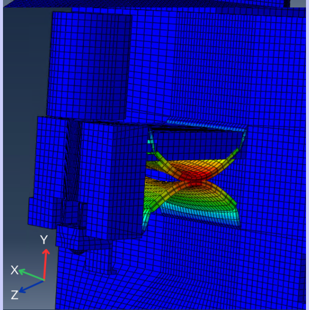	
2033 Hz	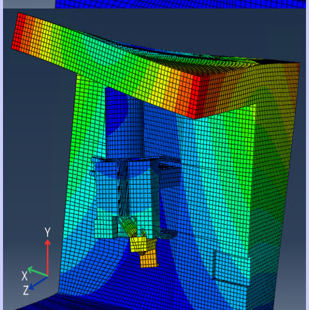	
2075 Hz	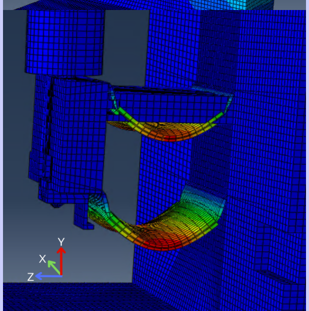	
No displacement	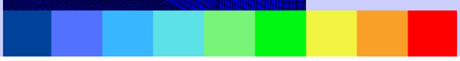	**Maximum displacement**

Table 6: Remaining eigenmodes with plotted mode shapes for upper system

FEM	**Mode shape**	**Estimation**
414 Hz	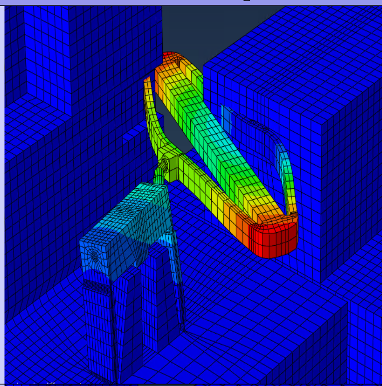	
625 Hz	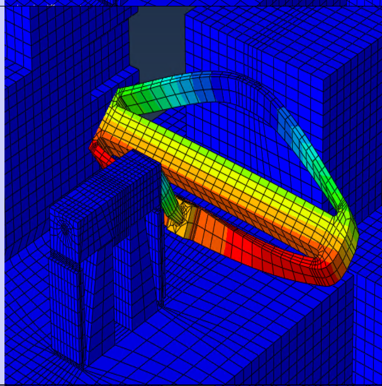	
657 Hz	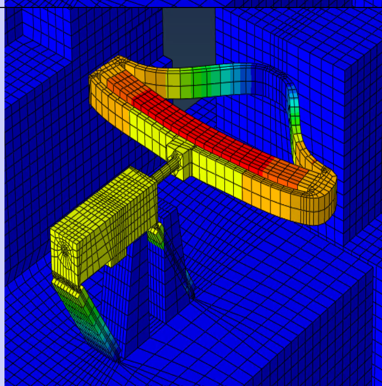	$M_{wire} = 0.007$ kg $M_{piezo} = 0.23$ kg $M_{flexure} = 0.049$ kg $K_{wire,x} = \frac{E\pi r^2}{L} = 22.62$ N/μm $C_{flexure,x} = \frac{24EI}{L^3}\frac{1}{(1-p^3)} = 17.5$ N/mm $C_{piezo,x} = 1.1$ N/μm $C_{eq} = \left(\frac{C_{wire,x}C_{flexure,x}C_{piezo,x}}{C_{wire,x}+C_{piezo,x}+C_{flexure,x}}\right)$ $f_x = \frac{1}{2\pi}\sqrt{\frac{C_{eq}}{M}} = 330$ Hz
No displacement		**Maximum displacement**

Table 7: Mode shapes and analytical solutions for lower system

FEM	Mode shape	Estimation
1496 Hz	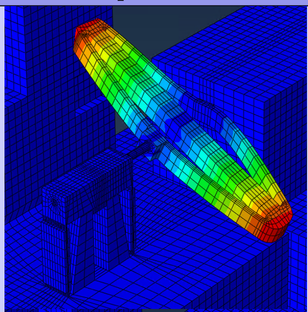	
1712 Hz	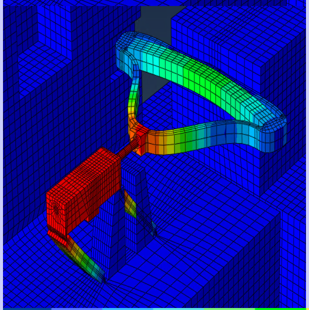	
No displacement	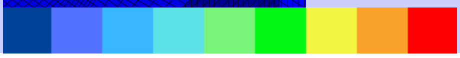	**Maximum displacement**

Table 8: Remaining eigenmodes with plotted mode shapes for lower system

4.5 Frequency response function

To find the natural frequencies of the system under dynamic loading conditions where the actuation force, normal force and friction coefficient is used as an input, A harmonic modal analysis is executed.

Initially, a static modal analysis is performed to find the natural frequencies of the system. After that, a predetermined actuator force is used to excite harmonic oscillation in the system over the bandwidth of natural frequencies present in the system. The result is the frequency spectrum of excited modes during operation. This gives a bandwidth on what frequencies will excite the system into vibration and which will not. Figure 32 shows the harmonic response of the lower mechanism with a 10 N actuation force, 5 N normal load and no friction while in contact. A sweep of several friction coefficients will be done to see what the response is in the frequency domain. The same will be done for the upper mechanism, which also holds the force flexure.

Naturally, there are many more modes present in the system, which we know from the modal analysis that was done on the entire system. However, these modes have not presented itself in figure 32 due to the force input given as input during the simulation. The force input was one-dimensional and applied at a single point. A random response analysis, which means shaking the entire system in all dimensions over a spectrum of frequencies, would display the full frequency response function (FRF) plot of the system. Such a plot could prove useful in determining the amplification in flexure or frame deflection as a result of resonance.

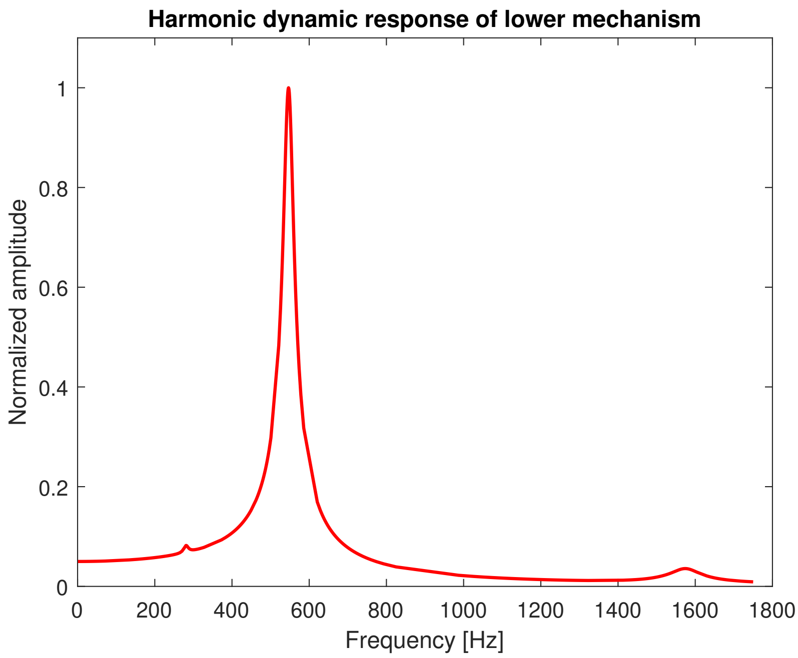

Figure 32: Steady state response lower mechanism

5 Contributing errors

It is important to consider contributing errors to the measurement accuracy of the friction force, normal force and position measurement. When errors are sufficiently small such that they do not exceed the total required accuracy, they can be neglected. If there are errors that possibly exceed the required accuracy, redesign might be necessary to minimize this error to ensure that the accuracy requirements are met.

5.1 Machining errors and misalignments

Inaccuracies in machining and alignment are inevitable. Machining offsets will cause misalignments when parts of the setup are connected to each other. After consulting with a machining specials at the TCO workshop at the University of twente, the following information was provided to quantify misalignment errors in to-be manufactured parts in the setup.

- 20 μm flatness per part is attainable
- A 30 μm gap is necessary for parts that need to fit or slide into one another
- A total relative alignment of 5 μm can between parts using sophisticated alignment equipment.

The aforementioned misalignments are quantified in force and displacement errors.

Horizontal motion misalignment error

- placement of piezo on frame (two axes 30 μm)
- placement of piezo on flexure (two axes 30 μm)
- placement of sinking horizontal flexure (two axes 30 μm)
- calculate offset loading in force for x-direction (displacement and angle) when things are not aligned.
- calculate offset loading when things are aligned

For the horizontal flexure, the fitting gap of 30 μm is a worst-case rotation of $tan^{-}1(\frac{30\mu m}{0.06m}) =$ 0.0307° around the y-axis in the zx-plane, resulting in a 0.0034% offset error in the force delivered by the piezo and thus the same holds for the position error according to Hooke's law as the stiffness remains the same.

For the vertical flexure, the fitting gap of 30 μm is a worst-case rotation of $tan^{-}1(\frac{30\mu m}{0.11m}) =$ 0.015° around the y-axis in the zx-plane, resulting in a 0.0017% offset error in the normal load delivered by the voice coil and thus the same holds for the position error according to Hooke's law as the stiffness remains the same.

5.2 Sensor errors

LIDA ... sensors 0.45 nm for lida sensors using 100-fold interpolation- 30 m/min - 25 kHz. The Y-flexure has 0.00717 N/μm stiffness, $F = K\delta x = 0.00717 \cdot 0.00045 = 3.225\mu N$, translates to 0.000322% error in the normal load with 0.1N applied.

The x-flexure has 0.45nm and a 0.000112% error in the position in x with 400μm stroke.

Lip 2 series sensor lip 12 - 0.4nm interpolation error - 0.12nm rms noise error - 120m/min transversing speed – 3.202 n/mu m stiffness $F = K\delta x = 3.202 \cdot 0.00052 = 1.665mN$, translates to 0.01665% error in case of the maximum friction force of 10N under static deflection.

Sensor errors in velocity and acceleration Once the position errors are quantified , an estimation must be made on the error in velocity and acceleration. From the definition of the derivative[28], velocity is approached by equation 70 as

$$v(t) \approx \frac{x(t+\delta t) - x(t)}{\delta t} \tag{70}$$

Here, $v(t)$ is the velocity, $x(t)$, t is the passed time and δt is the time between samples. The error δv resulting from numerical differentiation of the position is then defined by equation 71. It is shown that δv relates to the position error δx with a factor $\frac{2}{\delta t}$, meaning that a very small time between samples, results in a large error in δv.

$$\delta v = \frac{2\delta x}{\delta t} \tag{71}$$

Again taking the definition for the derivative, equation 72 is used to numerically integrate the velocity to get an approximation for the acceleration $a(t)$

$$a(t) \approx \frac{x(t+\delta t) - 2x(t) + x(t-\delta t)}{\delta t^2} \tag{72}$$

The error in the acceleration, δa is then calculated using equation 73. The relation between δx and δa is $\frac{4}{\delta t^2}$, meaning that a small time step δt results in an even larger error than δv.

$$\delta a = \frac{4\delta x}{\delta t^2} \tag{73}$$

The position, velocity and acceleration sensor error is most relevant for the Encoder used in for the horizontal flexure. The Lida optical encoder has an interpolation error of 0.45nm. The interpolation error will translate to errors in velocity and acceleration as well. A 25 kHz sampling frequency means that δt is 40 μs. Using equation 71, it is found that δv is 22.5 $\mu m s^{-1}$. Using equation 73, δa is found to be 1.12 ms^{-2}.

The LIP encoder used for measuring the deflection and calculating the velocity and acceleration for the force flexure has a combined error in the position measurement of 0.55nm. Using equation 71 and 73, this results in an error of respectively 0.0012 ms^{-1} and 2.08ms^{-2}. The encoder error in position and acceleration would result in a friction force measurement error of respectively 0.000208 N and 0.0719 N. It is seen that due to numerical differentiation, the resulting force error is increased drastically. To minimize this, filtering after differentiating once, and then again filtering after differentiating to get the acceleration can help to minimize the quadratic increase in the error.

5.3 Stiffness calibration force measurement system

You can discuss with Sip Jan from TCO about machining-related errors or tolerances.
After machining of the flexures, the flexure stiffness must be calibrated to ensure accurate force inputs for the actuators. A static load test using a postion sensor and precision weights to incrementally load the flexure is a very common way of calibrating flexure stiffness and linearity.

The error in the force calibration is subject to the measurement equipment used. In case of using the Lida .... encoder, the error in position measurement will be ... . Combined with using calibration weight of class M1[29], the error resulting from calibrating the stiffness of each flexure can be calculated by summing the cumulative error of the calibration weight and the optical encoder at the measured deflection. It would be desirable to calibrate the flexures up to their maximum operating stroke. For the y flexure, x flexure and force flexure this would respectively be 0.002m, 400 μm and 3.12 μm respectively.
All errors during the calibration procedure stem from:

- Error in the encoder: 0.4nm interpolation error when using Lida encoder over min and max disp.

- The precision the precision weights of class M1 is 0.1% at maximum.
- Ensured accuracy of encoder and scale of 5 μm

These three incidents result in an error in the calibration points. For all flexures in the setup, the stiffness is calibrated with a number of calibration weights. The To have a reference value for the measured stiffness over the whole Rms is then between expected theoretical value and maximum possible error Result is .... Newton V flex: 2 mm max, requiring a force of 14,35N, which translates to a calibration weight of 1.46 kg. Since the weight of the shuttle is 110gr, the deflection by its own weight is 0.15 mm. To reach a maximum deflection of 2 mm, an additional downward force of 13.27N or 1.35kg must be added.

The RMS error is determined by calculating the difference between an idealized theoretical spring force value and the measured spring force using precision weights and an optical position sensor.

The expected spring force, $F_{expected,i}$, is defined as follows.

$$F_{expected,i} = k_{theoretical} x_i \tag{74}$$

Here, $k_{theoretical}$ is determined by equation

$$\mathrm{RMS}_{\mathrm{error}} = \sqrt{\frac{1}{N}\sum_{i=1}^{N}\left(F_{expected,i} - F_{measured,i}\right)^2} \tag{75}$$

For the measured value, a linear fit is then used to express the measured stiffness over the entire stroke in the form of

$$F_{measured,i} = k_{fit} x_i + b \tag{76}$$

This way of defining the error as a result of the contributing possible errors during calibration is possible when the deflections can actually be measured. Since there is a limitation of purely theoretical quantification, the root sum of squares, RSS, will be used to quantify a possible error resulting from stiffness calibration of the flexures. This is calculated as Δ_{total} using equation 77.

$$\Delta_{total} = \sqrt{(\Delta A)^2 + (\Delta B)^2 + (\Delta C)^2 + (\Delta D)^2} \tag{77}$$

Where ΔA is the encoder error 0f of 0.4nm, which based on maximum deflection of the flexures translates to 0.0001% for the H-flexure, 0.0128% for the F-flexure and 0.00002% for the V-flexure.

ΔB is 0.1% inaccuracy associated with the calibration weights of class ΔC is the 5μm misalignment between the scale and optical center of the encoder. According to the spec sheet, this misalignment does not influence the measurement quality of the encoder. The total RSS is then defined using equation 77. For the H-flexure, F-flexure and V-flexure this respectively yields a rounded off error of 0.1% for all three flexures. For the F-flexure, this comes down to a 10 mN error based on a maximum deflection of 3.12 μm. This is too large.

5.4 Abbe errors

0.816 μrad for x flexure. The offset for the optical encoder for the x-flexure is 0.015m. Using equation 37, it shows that the Abbe error for this encoder is 12.24nm. This is an error of 0.003% for the displacement accuracy in the x-direction when taking the full stroke of 400 μm.

The Abbe offset between the force flexure and the accompanying optical encoder resulting from machining inaccuracy will be 30 μm worst-case. The rotation of the force flexure at maximum stroke is 3.38 μrad. This results in an Abbe error in the force measurement of 0.101nm, which translates to an absolute error of 0.32 mN and a

The relevant abbe error in the vertical flexure is resulting from combined shortening of the force flexure and the

5.5 Error of actuators

Amplified piezo actuator errors Errors in the amplified piezo actuator for facilitating movement in the x-direction of the lower flat specimen is most prominent due to hysteresis of the piezo actuator itself. If not compensated for, positioning inacurracy due to hysteresis is commonly between 10-15%. Piezoelectric transducer (PZT) hysteresis can be well-defined using a mathematical model like the Preisach, Prandtl-Ishlinskii or Bouc-Wen hysteresis model. The use of a feedforward controller in combination with a hysteresis model is found to repetitively deliver positioning with an error below 1% RMS [30][31].

Voice coil errors The most prominent error in a voice coil actuator is the occurrence of magnetic hysteresis, temperature dependent current and impedance, and eddy currents caused by self-inductance.

Joule heating of the voice coil is heating of the coil resulting from current running through a conductive material with nonzero resistance. Because of this, the Lorentz force delivered to the payload is decreased, as resistance in the coil increases with increasing temperature. When the voice coil makes 10000 reciprocating cycles of back-and-forth motion, the total heat buildup and Normal load reduction are, respectively $21.5°C$ and 0.79N. One cycle of movement takes 6.7 ms with a standstill of 10ms, meaning one cycle of back-and-forth motion takes 33.4 ms. multiplying this with 10000 cycles gives a rounded upward loading time of 6 minutes. 0.79N load reduction is a relative error of 7.9%, which is too much to be acceptable. A feedforward controller must be used to mitigate this error. Together with coil temperature measurement and the Energy balance equation describing the heat buildup and dissipation as a function of the applied current in the coil, the temperature dependent normal load error can be minimized to sub 0.5% error.

Remaining unpredictable nonlinear behaviour can be minimized using a PID controller. Again, errors of sub 0.5% in the normal load applied are realistic if the controller is tuned well.

5.6 Accumulated errors

Error	Contribution	Unit	Variable
Misalignment lower system	0.0034	%	X-position
X sensor	0.000112	%	X-position
APA error	1	%	X-position
Abbe error X flexure	0.003	%	X-position
Stiffness calibration X	0.1	%	X-Position
Misalignment upper system	0.0017	%	Normal load
Y sensor	0.000322	%	Normal load
Stiffness calibration Y	0.1	%	Normal load
Voice coil error	1	%	Normal load
Force sensor	0.01665	%	Friction
Stiffness calibration F	0.1	%	Friction
Abbe error F flexure	0.0003	%	Friction

Accumulated x-position error: 1.1104% of total stroke.
Accumulated error in normal load: 1.102%
Accumulated error in friction measurement: 0.14865% based on 10N deflection.

6 Discussion

In this report, a microtribometer is designed capable of measuring sliding friction of a ball-on-flat contact under high-accelerated sliding with high accuracy. The desire for the development of such a setup is justified by the existing research gap in phenomenologically characterizing friction under high-accelerated sliding. The proposed design process and results revealed critical insights in system behaviour, performance, and its limitations and the trade-offs that are made.

A fundamental strength in the design of the setup is the use of flexure-based positioning due to them being near-frictionless, backlash-free and thus highly deterministic. A reinforced parallel leaf spring was used to design the two independent 1 DOF mechanisms: one to deliver the normal load at the contact, and one to initiate accelerated sliding of the flat specimen. A parallel leaf spring proved to have a favourable stiffness-to-weight ratio. A friction force sensor was designed by using a parallel leaf spring combined with a optical encoder measuring the flexure deflection. Using a flexure based force transducer allowed for scalable force resolution to fit the desired use.

The decision to keep the moving mass in the accelerating part of the setup as low as possible, is based on the fact that a lower moving mass means that the peak force required by the used actuator is lower compared to a high moving mass. On top of that, a low moving mass requires less force to dampen transient oscillations, in turn aiding the accuracy of the measurement. Once the flexures, actuators, sensors and remaining components were chosen and put in the design of the setup, a modal analysis was done to test the transient dynamics of the system and see which bandwidth can be achieved for the actuators. The modal results showed that the designed support frames offer sufficient rigidity and thus a high eigenfrequency, preventing resonance building up over the duration of the measurement. Additionally, the lowest eigenfrequency of the lower system was found to be 414 Hz, potentially offering a high enough bandwidth for frequencies induced by the piezo actuator chosen for applying force in the x-direction. However, this must be verified by estimating the frequency content during operation of the piezo actuator. The lowest eigenfrequency of the top system is 31 Hz. The latter eigenfrequency was expected to be low as the flexure stiffness is low, while the total moving mass is relatively high. A feedback controller is an adequate solution to deal with resonance at 31 Hz.

The contributing errors in the system are identified and quantified. The most notable concerns are the RMS error of the sensor used to measure the force flexure deflection and the achievable positioning accuracy of the APA. Since the force flexure is designed to have a low response time, the stiffness of the flexure is high, resulting in a low deflection. Under low deflection, the RMS error becomes more significant, as this is a semi-static error.

6.1 Limitations and Recommendations

Throughout the design process, a number of limitations were identified, offering room for improvement. These improvements span over the force transducer, actuation of the horizontal sliding motion, modal dynamics and the machinability of the custom parts.

Force transducer

A primary limitation of the force transducer design is its high stiffness, which, while enabling rapid response and high resolution, requires a position sensor with minimal static errors, as these cannot be averaged out over time. It was found that the optical encoder has a RMS and interpolation error that is too high with the current flexure stiffness used. If one wants to keep the same response time, the weight of the flexure must come down such that the flexure stiffness can be slightly decreased, creating a larger deflection and in turn a larger signal-to-noise ratio.

Alternatively, selecting a material with a comparable strength-to-weight ratio but higher yield strain than AL 7075 could maintain response time while allowing for greater deflection.

Finally, one could choose to pick a position sensor with a lower static errors than the current optical encoder chosen. A capacitive probe combined with the CPL-490 amplifier from Lion Precision would be a viable option[32]. A error band of below 0.5% in the full-scale measuring range is achievable.

Horizontal Motion System

Open-loop control of the APA actuator results in insufficient accuracy, primarily due to hysteresis. It would be required to at least use a feedforward controller to reduce the position error resulting from hysteresis. Creep, the time-dependent drift resulting from a voltage supplied to the APA, is another non-linear effect that must be controlled to maintain accuracy. A feedback controller will likely have to be implored, as a level of unpredictability is involved when using a APA.

In terms of actuation, a VCA is preferable over APA actuators, which exhibit significant hysteresis unless compensated. A VCA experiences some magnetic hysteresis, but the order of magnitude of this hysteresis is minute. Hysteresis compensation of a APA through a feedforward controller is complex and computationally expensive, potentially exceeding the available pause time between oscillations. A VCA experiences Joule heating, back EMF, saturation, and Eddy currents during dynamic operation. These phenomena cause inaccuracy if left uncompensated. However, these phenomena are all measurable and thus viable to compensate in order to achieve accurate tangential force delivery.

From a structural dynamics standpoint, a VCA is superior over an APA since a VCA is mechanically decoupled from frame, mitigating the necessity for a stiff frame that would otherwise be required when using an APA. This effectively makes the force balance for achieving desired actuation much simpler.

Modal analysis

Modes 1 and 2, occurring at 414 Hz and 625 Hz respectively, appear to originate from the wire flexure 7. It would be useful to see if the APA is compliant enough in the y-direction such that the wire flexure can be omitted from the setup, effectively increasing the bandwidth of movement in the x-direction. This can be done by doing a bend-displacement test of the APA in FEM.
The first eigenmode of 31 Hz in the upper system, plotted in table 5, is low and expected since the voice coil has no static stiffness or damping. A high frequency feedback controller can be used to deal with resonance occurring at 31 Hz. Since the optical encoder used combined with the voice coil has a clock speed of 25 kHz and accuracy of 0.45 nm, the encoder will not contribute much to the total tracking error. Adding a notch filter could help mitigate resonance at 31 HZ, in addition to a feedback controller.

Machining

The flexures and the frames will be machined using wire EDM and CNC machining. The material choice is mainly based on performance of the setup, but the machinability and possible added complexity machining certain materials must be considered as well. Using steel 316 or 304 for the frames, instead of stainless steel 216, could reduce internal stress and minimize the need for post-processing to achieve alignment within 5 μm. Less post-processing effectively means less cost. In case that the cost of the remaining components leaves a smaller budget for machining parts than expected, considering the use of materials with lower internal stress will be a good option to consider to save cost.

Additionally, the flexures are manufactured using wire EDM. At narrow interfaces like the flexural parts of the reinforced parallel leaf springs, warping thermal warping might occur, which could potentially change the stiffness of the flexure and decrease its lifespan. Therefore, it is essential to assess the severity of thermal warping before proceeding with manufacturing.

7 Conclusions

In this report, a conceptual design is made for a novel microtribometer capable of measuring sliding friction under high acceleration with high accuracy. The system makes use of flexure-based positioning mechanisms and high-speed sensing to allow for accurate force control. The proposed system and its components were analysed. Most requirements are met, with a few requiring design adjustments in order for the requirements to be met. Shortcomings and limitations are discussed, followed by recommendations for future development. Finally, it is concluded that the proposed design is viable.

8 Appendix

A Rotational stiffness parallel leaf

figure 33 shows the free body diagram of the force measuring flexure mechanism. It is important to consider that the placement of the centre of the optical encoder lens, the optical centre, is moved to be in-plane in the zx-plane of the glass bead. This way, the Abbe error in the x-direction will be zero because there is zero Abbe offset. However, the rotation of the force measuring flexure remains.

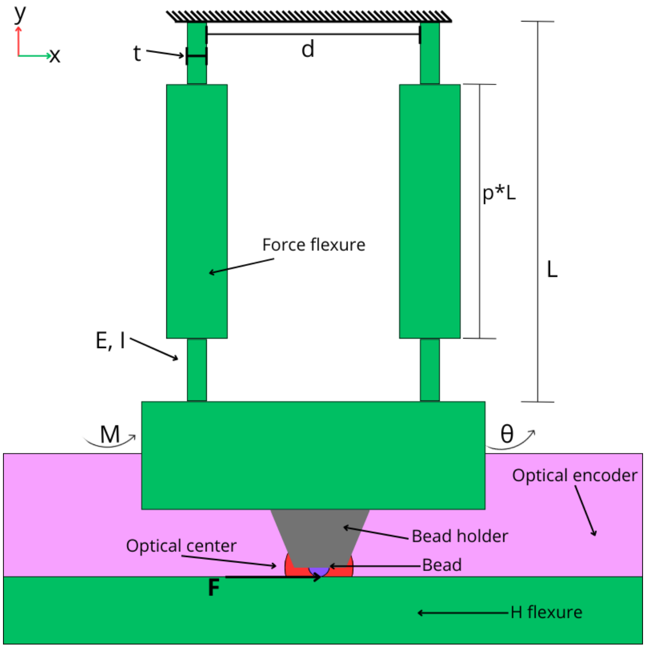

Figure 33: Schematic diagram of parallel leaf with bead holder

B Abbe error

A simple schematic diagram is shown in figure 34 to show what the relevant parameters are in determining and minimizing the Abbe error.

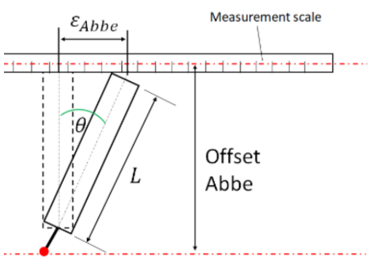

Figure 34: Schematic depiction of abbe error

C Mode shapes

In table 9, the plotted modeshapes of the individual parts in the system are plotted.

Part	Mode 1	Mode 2	Mode 3	Mode 4
H flexure	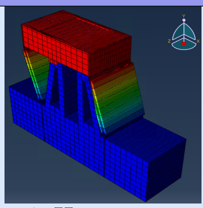 237 Hz	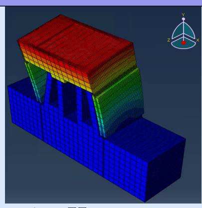 2370 Hz	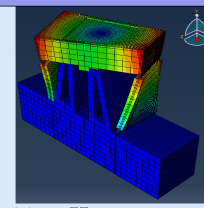 4496 Hz	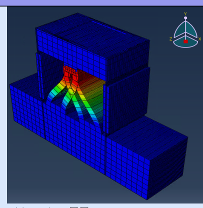 4727 Hz
V flexure	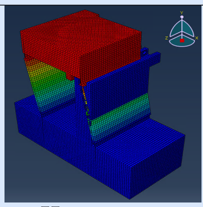 36 Hz	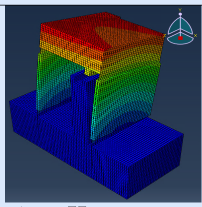 1702 Hz	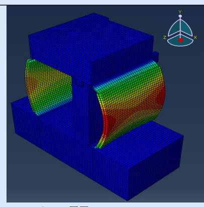 2049 Hz	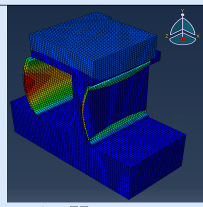 2049 Hz
Force flexure	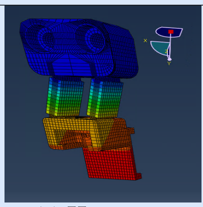 2844 Hz	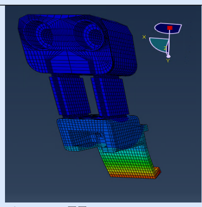 4202 Hz	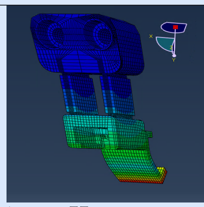 7881 Hz	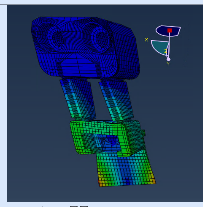 9242 Hz
Wire flexure	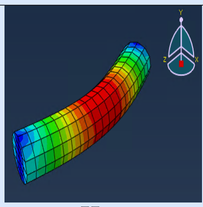 18620 Hz	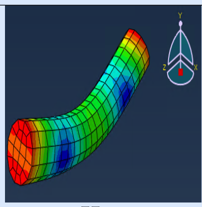 39933 Hz	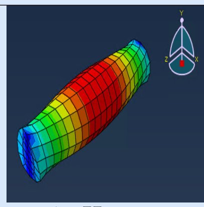 66543 Hz	
Piezo frame	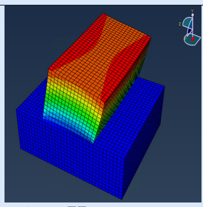 2403 Hz	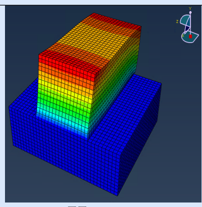 2802 Hz	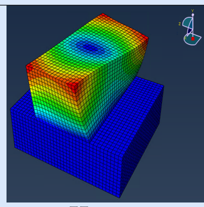 2956 Hz	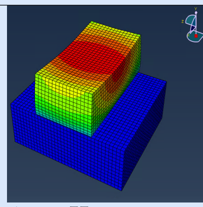 4631 Hz
Big frame	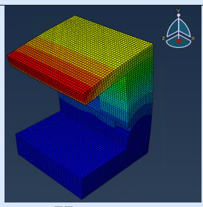 785 Hz	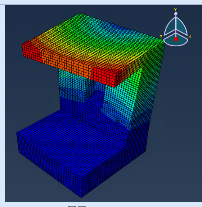 1333 Hz	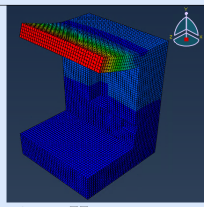 1732 Hz	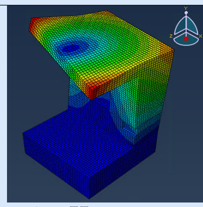 1976 Hz
Piezo actuator	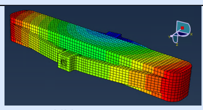 155 Hz	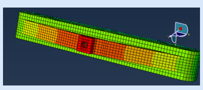 189 Hz	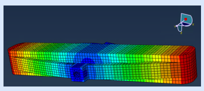 494 Hz	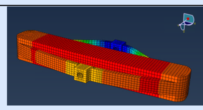 553 Hz

Table 9: Mode shapes of the individual parts in the system

D Budget

The initial budget is set at €25000. Table 10 contains the chosen components including its price to keep track of the money that would have to be spent in case of choosing to go further with the setup.

Part	Type	Url	Price
Position sensor H flexure	AK LIDA 48 optical encoder		€625
Position sensor F flexure	LIP 201 optical encoder		€2355
Actuator horizontal motion	APA500L + LA75c amplifier		€7500
Readout position sensors	NI (CHECK exact one)		€2100
Machined parts in setup			€3100
Actuator vertical system			
Position sensor V flexure	AK LIDA 48 optical encoder		€625
Frame for piezo actuator			
	Given budget:	€25000	
	Total cost:	€15680	

Table 10: Table containing chosen components including pricing

E Fatigue

The SN-curve of 7075 aluminium alloy is used to determine the fatigue stress for the amount of cycles the flexures are exposed to during their lifetime. The SN-curve is shown in figure 35.

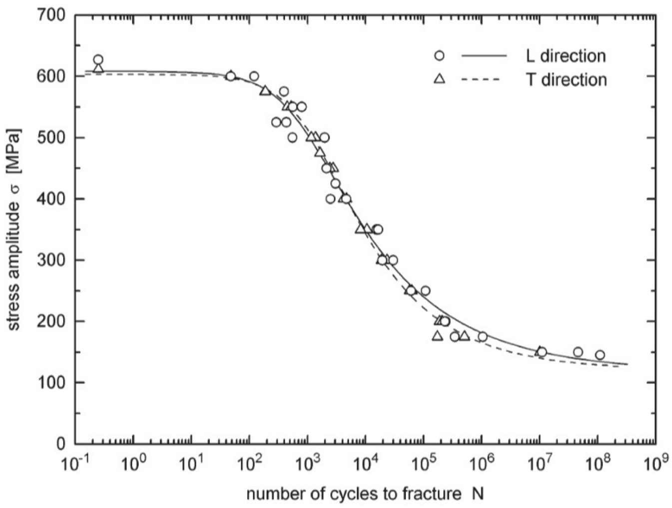

Figure 35: SN-curve of 7075 aluminium alloy [33]

F Granta table for material selection

The table below shows how the density of several materials compares to their own respective yield strength. The closer a material is to the top left corner, the bigger their strength to weight ratio will be, which is desirable for designing a strong and lightweight component.

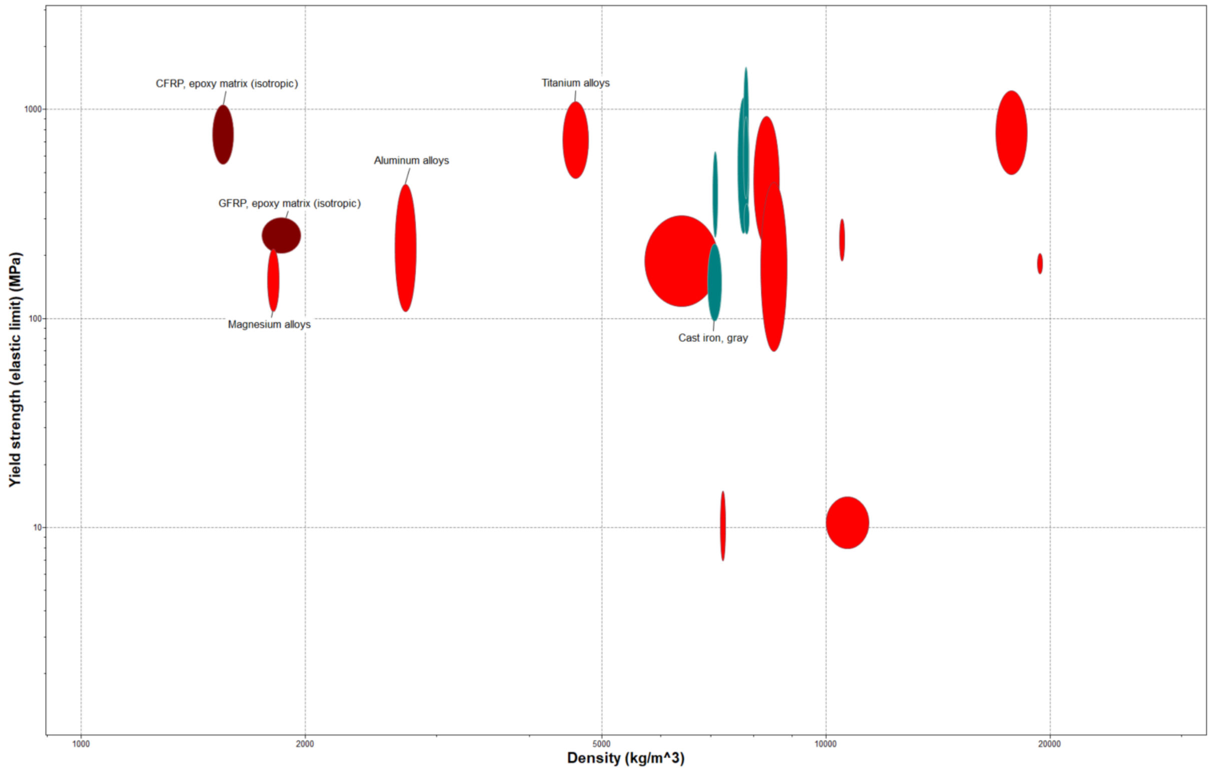

Figure 36: Granta table showing density compared to yield strength of different materials

G Inertia

Table 11 is a comparison of calculating the second moment of area of a simple geometry by hand, compared to SolidWorks own calculation tool. This is done to validate that SolidWorks accurately determines the second moment of area of more exotic geometries as well.

SolidWorks	**Approximation**
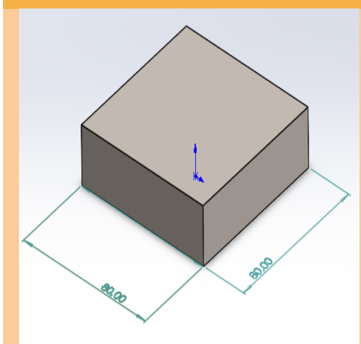	$M = 1.008kg$ $I = \frac{1}{12}M(a^2 + b^2)$ a = b = 0.08m
$I = 0.0010731kgm^2$	$I = 0.0010752kgm^2$

Table 11: Comparison of calculating inertia with SolidWorks and pen on paper approximation

H Granular assembly setup schematic

The normal stress applied on the granular assembly ranges from 8 to 40 MPa. Consequently, the outer and inner radii of these rings are 50 and 35 mm. This accounts for a contact area A of 0.004 m^2. The grain size varies between 50 and 500 μm. The densest packing fraction φ of

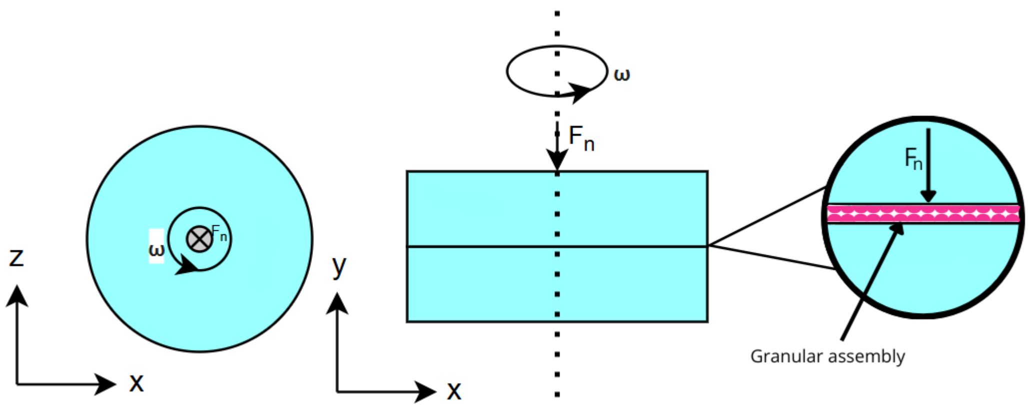

Figure 37: Schematic view of grain on grain contact in existing rotary setup

a hexagonal lattice filled with circles is approximately 0.9 [34]. Taking the packing fraction into account, the normal stress σ_n applied on the granular assembly is defined in equation 78.

$$\sigma_n = \frac{F_n}{A\varphi} \tag{78}$$

Rewriting yields the normal load F_n in equation 79.

$$F_n = \sigma_n A\varphi \tag{79}$$

It is found that the force applied is 28.8 kN for 8 MPa of stress. 144 kN is applied with 40 MPa of stress. For a singular 50 μm grain in contact, a force of respectively 0.0628 and 0.248 N is applied. For a 500 μm grain in contact, the normal load is 6.28 and 24.8 N respectively.

I Voice coil actuator for movement in x-direction

The movement in the x-direction is facilitated by an amplified piezo actuator. A voice coil would also be a viable option. Figure 38 shows the required voltage and current over time depending on the desired velocity profile of the lower specimen. Figure 39 shows the required power in time based on the drawn current and supplied voltage.

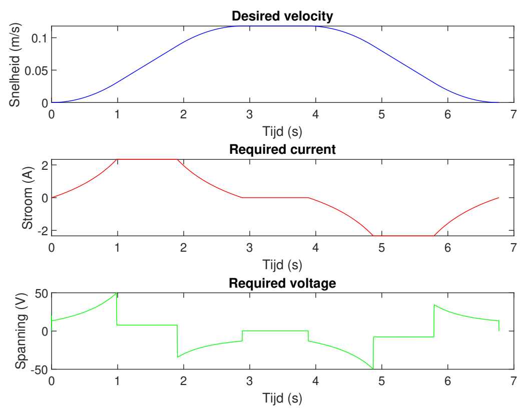

Figure 38: Velocity, current, and voltage required for the voice coil

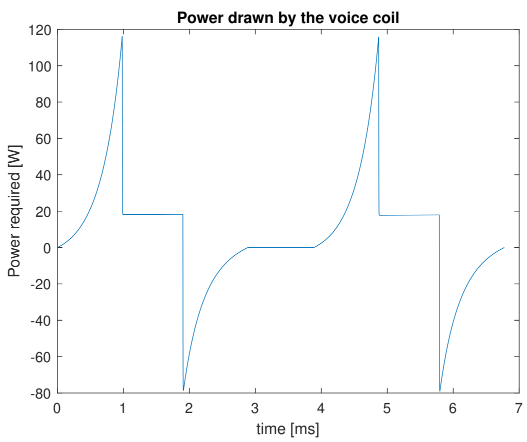

Figure 39: Power drawn by the voice coil over time

References

[1] H. Hertz, "Über die berührung fester elastischer körper," Journal für die reine und angewandte Mathematik, vol. 92, pp. 156–171, 1882. [Online]. Available: https://en.wikipedia.org/wiki/Contact_mechanics

[2] J. Wilhayn and M. Heß, "Frictional energy dissipation in partial slip contacts of axisymmetric power-law graded elastic solids under oscillating tangential loads: Effect of the geometry and the in-depth grading," Mathematics, vol. 10, no. 19, p. 3641, Oct. 2022.

[3] "Chapter 8. models of friction," https://mogi.bme.hu/TAMOP/robot_applications/ch07.html, [Accessed 18-04-2025].

[4] J. Woodhouse, T. Putelat, and A. McKay, "Are there reliable constitutive laws for dynamic friction?" Philos. Trans. A Math. Phys. Eng. Sci., vol. 373, no. 2051, p. 20140401, Sep. 2015.

[5] G. Rill, T. Schaeffer, and M. Schuderer, "LuGre or not LuGre," Multibody Syst. Dyn., vol. 60, no. 2, pp. 191–218, Feb. 2024.

[6] "Chapter8.4.2.5 modified dahl model," https://mogi.bme.hu/TAMOP/robot_applications/ch07.html#ch-8.4.2.5, [Accessed 24-04-2025].

[7] "Product - Multi Capability Pin on Disk Tribometer (POD 4.0) — lp.ducom.com," https://lp.ducom.com/pod4.0-1, [Accessed 25-05-2025].

[8] "SRV®5 Tribometer • Optimol Instruments Prüftechnik GmbH — optimol-instruments.de," https://optimol-instruments.de/en/products/srv5/, [Accessed 25-05-2025].

[9] "Tribometer — In-line Profiler — Rtec Instruments — rtec-instruments.com," https://rtec-instruments.com/tribometer/universal-tribometer/?gad_campaignid=1698695032, [Accessed 25-05-2025].

[10] J. L. Dion, G. Chevallier, O. Penas, and F. Renaud, "A new multicontact tribometer for deterministic dynamic friction identification," Wear, vol. 300, no. 1-2, pp. 126–135, Mar. 2013.

[11] I. S. Y. Ku, T. Reddyhoff, J. H. Choo, A. S. Holmes, and H. A. Spikes, "A novel tribometer for the measurement of friction in MEMS," Tribol. Int., vol. 43, no. 5-6, pp. 1087–1090, May 2010.

[12] M. Kosinskiy, S. I.-U. Ahmed, Y. Liu, and J. A. Schaefer, "A compact reciprocating vacuum microtribometer," Tribol. Int., vol. 56, pp. 81–88, Dec. 2012.

[13] L. R. Tamatam, D. Botto, and S. Zucca, "A novel test rig to study the effect of fretting wear on the forced response dynamics with a friction contact," Nonlinear Dyn., vol. 105, no. 2, pp. 1405–1426, Jul. 2021.

[14] P. Raut, A. S. Rao, P. Waghmare, and D. Baviskar, "High precision flexural mechanisms for scanning applications: A comprehensive review," gengpi, vol. 5, no. 2, pp. 1491–1497, Feb. 2024.

[15] S. M. H. Benabdallah, "Reciprocating sliding friction and wear test apparatus," Polym. Test., vol. 9, no. 3, pp. 195–211, Jan. 1990.

[16] "Soda lime glass — continentaltrade.com.pl," https://www.continentaltrade.com.pl/en/our-offer/technical-glass/types-of-materials/soda-lime-glass, [Accessed 31-05-2025].

[17] P. D. E. Ltd. (2024) Hertzian contact explainedl description. [Online]. Available: https://product-development-engineers.com/2024/09/24/hertzian-contact-explained/

[18] "Leaf spring/flexure: Reinforced," Available at https://www.jpe-innovations.com/precision-point/leaf-spring-flexure-reinforced/.

[19] Heidenhain, "Exposed linear encoders," https://www.heidenhain.com/fileadmin/pdf/en/01_Products/Prospekte/PR_Exposed_Linear_Encoders_ID208960_en.pdf.

[20] A. user manual. Hourglassing and shear locking – what are they and why does it matter? Accessed: 04-03-2025. [Online]. Available: https://www.fidelisfea.com/post/hourglassing-and-shear-locking-what-are-they-and-why-does-it-matter

[21] C. Technologies. Apa500l. Accessed: 01-12-2025. [Online]. Available: https://cedrat-technologies.com/produit/apa500l

[22] W. Syam. Ten types of dimensional and geometrical measurement error. Accessed: 02-02-2025. [Online]. Available: https://www.wasyresearch.com/ten-types-of-dimensional-and-geometrical-measurement-error

[23] "Voice Coil Actuator - NCC03-15-050-2X - H2W Technologies — h2wtech.com," https://www.h2wtech.com/product/voice-coil-actuators/NCC03-15-050-2X, [Accessed 31-05-2025].

[24] H. He, Q. Qiao, T. Xiao, J. Yu, and S. H. Kim, "Effect of humidity on friction, wear, and plastic deformation during nanoscratch of soda lime silica glass," J. Am. Ceram. Soc., vol. 105, no. 2, pp. 1367–1374, Feb. 2022.

[25] A. user manual. Natural frequency extraction. Accessed: 03-03-2025. [Online]. Available: https://classes.engineering.wustl.edu/2009/spring/mase5513/abaqus/docs/v6.6/books/usb/default.htm?startat=pt03ch06s03at09.html

[26] A. benchmark manual. 1.4.14 residual modes for modal response analysis. Accessed: 04-03-2025. [Online]. Available: https://classes.engineering.wustl.edu/2009/spring/mase5513/abaqus/docs/v6.6/books/bmk/default.htm?startat=ch01s04ach50.html

[27] "Leaf spring/flexure: Reinforced - JPE — jpe-innovations.com," https://www.jpe-innovations.com/precision-point/leaf-spring-flexure-reinforced/, [Accessed 23-04-2025].

[28] "Calculus I - The Definition of the Derivative — tutorial.math.lamar.edu," https://tutorial.math.lamar.edu/classes/calci/defnofderivative.aspx, [Accessed 12-05-2025].

[29] "Cilindergewichten, roestvrij staal, klasse M1 - Henk Maas Weegschalen — henkmaas.nl," https://www.henkmaas.nl/products/cilindergewichten-roestvrij-staal-klasse-m1/#tab1, [Accessed 14-05-2025].

[30] M.-J. Jang, C.-L. Chen, and J.-R. Lee, "Modeling and control of a piezoelectric actuator driven system with asymmetric hysteresis," J. Franklin Inst., vol. 346, no. 1, pp. 17–32, Feb. 2009.

[31] Z. Yu, Y. Wu, Z. Fang, and H. Sun, "Modeling and compensation of hysteresis in piezoelectric actuators," Heliyon, vol. 6, no. 5, p. e03999, May 2020.

[32] "lionprecision.com," https://www.lionprecision.com/wp-content/uploads/2022/07/Brochure-CPL490.pdf, [Accessed 17-06-2025].

[33] J. Zapletal, S. Vechet, J. Kohout, and P. Liskutin, "Fatigue lifetime of 7075 aluminium alloy from ultimate tensile strength to permanent fatigue limit," Komunikacie, vol. 11, pp. 17–21, 03 2009.

[34] N.A. Circle packing. Accessed: 11-03-2025. [Online]. Available: https://en.wikipedia.org/wiki/Circle_packing

[35] WSU, "Pipeline pressure loss," Available at http://irrigation.wsu.edu/Content/Calculators/General/Pipeline-Pressure-Loss.php.

[36] N.A. Soda lime glass. Accessed: 14-03-2025. [Online]. Available: https://calcdevice.com/sphere-and-flat-plate-contact-id40.html

[37] ——. Non-comm dc voice coil linear actuator - ncc03-15-050-2h. Accessed: 28-03-2025. [Online]. Available: https://www.h2wtech.com/product/voice-coil-actuators/NCC03-15-050-2H

[38] D. Gangloff, A. Bylinskii, I. Counts, W. Jhe, and V. Vuletić, "Velocity tuning of friction with two trapped atoms," Nature Physics, vol. 11, no. 11, pp. 915–919, Nov 2015. [Online]. Available: https://doi.org/10.1038/nphys3459

[39] M. Yahiaoui, E. Rigaud, D. Mazuyer, and J. Cayer-Barrioz, "Forced oscillations dynamic tribometer with real-time insights of lubricated interfaces," Rev. Sci. Instrum., vol. 88, no. 3, p. 035101, Mar. 2017.

[40] J.-J. Arnoux, G. Sutter, G. List, and A. Molinari, "Friction experiments for dynamical coefficient measurement," Advances in Tribology, vol. 2011, 01 2011.

[41] "Ball-on-flat tests — Friction and Wear in Engineering Class Notes — Fiveable — library.fiveable.me," https://library.fiveable.me/friction-and-wear-in-engineering/unit-9/ball-on-flat-tests/study-guide/KeaRMPweGT4patM7, [Accessed 16-04-2025].

[42] "Methods Used for Friction Testing — microtribodynamics.engr.tamu.edu," https://microtribodynamics.engr.tamu.edu/methods-used-for-friction-testing/, [Accessed 16-04-2025].

[43] E. N. Brett Sanborn, Bo Song, "Development of a new method to investigate the dynamic friction behavior of interfaces using a kolsky tension bar," https://www.osti.gov/servlets/purl/1411602, [Accessed 16-04-2025].

[44] D. J. Aldabagh, T. L. Alzubadi, and A. F. Alhuwaizi, "Tribology of coated 316L SS by various nanoparticles," Int. J. Biomater., vol. 2023, p. 6676473, Aug. 2023.

[45] O. M. Braun and M. Peyrard, "Dependence of kinetic friction on velocity: master equation approach," Phys. Rev. E Stat. Nonlin. Soft Matter Phys., vol. 83, no. 4 Pt 2, p. 046129, Apr. 2011.